International Journal of Heat and Mass Transfer 52 (2009) 5849–5866

Contents lists available at ScienceDirect

International Journal of Heat and Mass Transfer

journal homepage: www.elsevier.com/locate/ijhmt

Analysis on multiplicity and stability of convective heat transfer in tightly curved rectangular ducts

Fang Liu [a], Liqiu Wang [b,*]

[a] Field Diagnostic Services, Inc., 446 Lincoln Highway, Fairless Hills, PA 19030, USA
[b] Department of Mechanical Engineering, The University of Hong Kong, Pokfulam Road, Hong Kong

ARTICLE INFO

Article history:
Received 11 March 2009
Received in revised form 31 July 2009
Accepted 31 July 2009
Available online 18 September 2009

Keywords:
Multiplicity
Stability
Hilbert spectral analysis
Forced convection
Curved duct

ABSTRACT

The present work is on bifurcation and stability of fully-developed forced convection in a tightly curved rectangular duct. Seven symmetric and four asymmetric solution branches were found. The physical mechanism and driving forces for generating various flow structures are discussed. The flow stability on various branches is determined by direct transient computation on dynamic responses of the multiple solutions. As Dean number increases, finite random disturbances lead the flows from a stable steady state to another stable steady state, a periodic oscillation, an intermittent oscillation, another periodic oscillation and a chaotic oscillation. The features of flow oscillations are examined by Hilbert spectral analysis. The mean friction factor and the mean Nusselt number are obtained for all physically-realizable flows. A significant enhancement of heat transfer can be achieved at the expense of a slight increase of flow friction.

1. Introduction

The present work addresses the fully-developed bifurcation and stability of the forced convection in a tightly curved rectangular duct with large aspect ratio (Dean Problem). Flows through a curved rectangular duct have attracted considerable attention because of its numerous applications in chemical and mechanical engineering. For example, curved rectangular passages are extensively used in heat exchangers, ventilators, gas turbines, aircraft intakes and centrifugal pumps. Studies of flows through curved rectangular ducts with various aspect ratios have been made experimentally and numerically. Cheng and Akiyama [1] employed aspect ratio ranging from 0.2 to 5 and found the secondary flow. Yee et al. [2] examined numerically steady laminar flows in ducts with aspect ratios of 0.33, 1 and 3 under the constant temperature boundary conditions. Komiyama et al. [3] numerically studied secondary flows and predicted Nusselt numbers in curved ducts of aspect ratios from 0.8 to 5. Ligrani and Niver [4] conducted experiments for the ducts with aspect ratios varying from 1 to 40. Thangam and Hur [5] made investigation of laminar secondary flows. Finlay and Nandakumar [6] studied the flow in the ducts with large aspect ratios (about 20 and 30) by the perturbation method. For the ducts of aspect ratio 40, Ligrani et al. [7] found that external heating at the outer wall affect the formation of secondary vortices more strongly than the case of heating at the inner wall. Chandratilleke and Nursubyakto [8] studied secondary flows through curved rectangular ducts of aspect ratios from 1 to 8. The number of Dean vortices is strongly affected by the duct aspect ratio. Convective heat transfer is significantly enhanced by the secondary flow, particularly when the Dean vortices appear at the outer wall.

Yanase and Nishiyama [9] found multiple solutions of the flow through a curved duct of large curvature ratio. They obtained two kinds of solutions: the two-cell solution and the four-cell solution for the same aspect ratio from 3.02 to 5. A comprehensive bifurcation study of laminar flows through a curved rectangular duct was made by Yanase et al. [10] for a wide range of aspect ratio without thermal effect. It was found that more and more steady solutions will appear as the aspect ratio increases and the flows tended to have a larger number of Dean vortices as streamwise velocity increases [10].

Dennis and Ng [11], Nandakumar and Masliyah [12] and Yanase et al. [13] made the study of dual flow solutions. Winters [14] made a detail investigation on the flow through a curved rectangular duct of aspect ratio from 1 to 2. The locations of limit points and symmetry-breaking bifurcation points change as the aspect ratio varies. As aspect ratio increases beyond 1.426, the solution structure changes: the two-cell flow branch becomes continuous at all axial pressure gradients and the secondary four-cell branch is

* Corresponding author. Address: Department of Mechanical Engineering, The University of Hong Kong, Pokfulam Road, Hong Kong. Tel.: +852 2859 7908; fax: +852 2858 5415.
E-mail address: lqwang@hku.hk (L.Q. Wang).

0017-9310/$ - see front matter © 2009 Elsevier Ltd. All rights reserved.
doi:10.1016/j.ijheatmasstransfer.2009.07.019

Nomenclature

a	duct width
b	duct height
$c_1 = -\frac{\partial P}{R_c \partial \phi}$	streamwise pressure gradient
$c_2 = \frac{\partial T}{R_c \partial \phi}$	streamwise temperature gradient
$d_h = 2ab/(a+b)$	hydrodynamic diameter
$De = Re\sqrt{\sigma}$	Dean number
$Dk = \frac{\sigma d_h W_1}{4\nu}$	pseudo-Dean number
$(fRe)_0$	average product of friction factor and Reynolds number for the straight ducts
$(fRe)_L$	local product of friction factor and Reynolds number
fRe	average product of friction factor and Reynolds number
Nu_0	average Nusselt number for the straight ducts
Nu_L	local Nusselt number
Nu	average Nusselt number
$p = \frac{P}{\rho(\nu/d_h)^2}$	dimensionless pressure
P	pressure of the fluid
$\Pr = \frac{\nu}{\alpha}$	Prandtl number of the fluid
$r = \frac{R}{d_h}$	dimensionless coordinates
R	coordinate
R_c	curvature radius
$\mathrm{Re} = \frac{d_h W_m}{\nu}$	Reynolds number
t	time
T	temperature of the fluid
T_w	wall temperature
$u = \frac{d_h U}{\nu}$	dimensionless velocity component along R-direction
U	velocity component along R-direction
$v = \frac{d_h V}{\nu}$	dimensionless velocity component along Z-direction
V	velocity component along Z- direction
$w = \frac{W}{W_1}$	dimensionless velocity component along ϕ-direction
W	velocity component along ϕ-direction
w_m	mean streamwise velocity
$W_1 = \frac{d_h^2 c_1}{\mu}$	representative streamwise velocity
$\boldsymbol{y}$	dependent-variable vector
$z = \frac{Z}{d_h}$	dimensionless coordinates
Z	coordinate

Greek Symbols

α	thermal diffusivity
$\Delta T = Pr\, d_h c_2$	representative temperature difference
μ	viscosity of the fluid
ν	kinematic viscosity;
ρ	density of the fluid;
$\gamma = \frac{b}{a}$	aspect ratio of rectangular cross section
$\theta = \frac{T_W - T}{T}$	dimensionless temperature of the fluid
θ_b	dimensionless bulk temperature of the fluid
θ_m	mean dimensionless temperature of the fluid
$\sigma = \frac{d_h}{R_c}$	curvature ratio of the duct
$\tau = \frac{t}{\nu/d_h^2}$	dimensionless time
ϕ	coordinate
$\psi_{\max}$	maximum value of secondary flow stream function

completely disconnected from the primary two-cell branch. All solutions except the primary two-cell flow are predicted to be unstable. Nandakumar and Weinitschke [15] also observed the change in connectivity of the solution branches past the transcritical points. This stimulates the present work to detail the flow bifurcation in curved ducts with a larger aspect ratio.

Yanase et al. [16] and Yanase et al. [17] studied numerically the flows through a curved rectangular duct with an aspect ratio of 2 by the spectral method with and without a temperature difference between the outer and inner walls. There exist three solution branches for the isothermal case (two symmetric and one asymmetric) and five solution branches for non-isothermal case (one symmetric and four asymmetric) at different Grashof number. With an increase in Dean number, the flow evolves from a stable state to a periodic flow and then to a chaotic state. However, no study has been found on the flow bifurcation and stability in curved ducts with a large aspect ratio up to 10 in the literature. Furthermore, the study on physical mechanism and driving forces for generating various flow structure as well as the characteristics of flow oscillations is very limited.

Therefore, the objective of this study are: (a) to make a relatively comprehensive study on the flow bifurcation and stability for the laminar forced convection in tightly curved rectangular ducts of curvature ratio 0.5 and aspect ratio 10 (Fig. 1), (b) to examine the physical mechanism and driving forces for generating various flow structures, and (c) to make spectral analysis on the features of flow oscillations.

2. Governing equations and numerical methods

Consider hydrodynamically and thermally fully-developed laminar flow in tightly curved ducts of curvature ratio 0.5 and aspect ratios 10 (Fig. 1). The finite pitch effect is not considered. Properties of the fluid are taken to be constant. The gravitational force is combined with the pressure term. For the the coordinate system (R, Z, ϕ) in Fig. 1, the governing equations read [18–20],

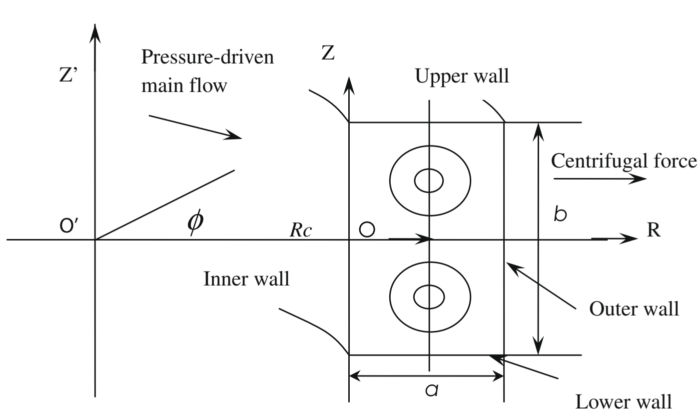

Fig. 1. Physical problem and coordinate system.

Continuity equation

$$\frac{\partial U}{\partial R}+\frac{U}{R_C-a/2+R}+\frac{\partial V}{\partial Z}=0 \tag{1}$$

Momentum equations:

$$\frac{\nu^2}{d_h^4}\frac{\partial U}{\partial t}+\underbrace{U\overset{①}{\frac{\partial U}{\partial R}}+V\frac{\partial U}{\partial Z}}-\underbrace{\overset{②}{\frac{W^2}{R_C-a/2+R}}} = -\underbrace{\frac{1}{\rho}\frac{\partial P}{\partial R}}_{③}+\underbrace{\nu\left[\frac{\partial^2 U}{\partial R^2}+\frac{\partial^2 U}{\partial Z^2}+\frac{1}{R_C-a/2+R}\frac{\partial U}{\partial R}-\frac{U}{(R_C-a/2+R)^2}\right]}_{④} \tag{2}$$

$$\frac{\nu^2}{d_h^4}\frac{\partial V}{\partial t}+\underbrace{U\frac{\partial V}{\partial R}+V\frac{\partial V}{\partial Z}}_{①}=-\underbrace{\frac{1}{\rho}\frac{\partial P}{\partial Z}}_{③}+\underbrace{\nu\left(\frac{\partial^2 V}{\partial R^2}+\frac{\partial^2 V}{\partial Z^2}+\frac{1}{R_C-a/2+R}\frac{\partial V}{\partial R}\right)}_{④} \tag{3}$$

$$\frac{\nu^2}{d_h^4}\frac{\partial W}{\partial t}+\underbrace{U\frac{\partial W}{\partial R}+V\overset{①}{\frac{\partial W}{\partial Z}}+\frac{UW}{R_C-a/2+R}}=-\underbrace{\overset{③}{\frac{1}{\rho(R_C-a/2+R)}}\frac{\partial P}{\partial \phi}}+\underbrace{\nu\left(\frac{\partial^2 W}{\partial R^2}+\frac{\partial^2 W}{\partial Z^2}+\frac{1}{R_C-a/2+R}\frac{\partial W}{\partial R}-\frac{W}{(R_C-a/2+R)^2}\right)}_{④} \tag{4}$$

Energy equation:

$$\frac{\nu^2}{d_h^4}\frac{\partial T}{\partial t}+U\frac{\partial T}{\partial R}+V\frac{\partial T}{\partial Z}+\frac{W}{R_C-a/2+R}\frac{\partial T}{\partial \phi} = \alpha\left(\frac{\partial^2 T}{\partial R^2}+\frac{\partial^2 T}{\partial Z^2}+\frac{1}{R_C-a/2+R}\frac{\partial T}{\partial R}\right) \tag{5}$$

where the terms labeled by ①, ②, ③ and ④ are the inertial force, centrifugal force, pressure and viscous force, respectively. Their dimensionless form is [18–20],

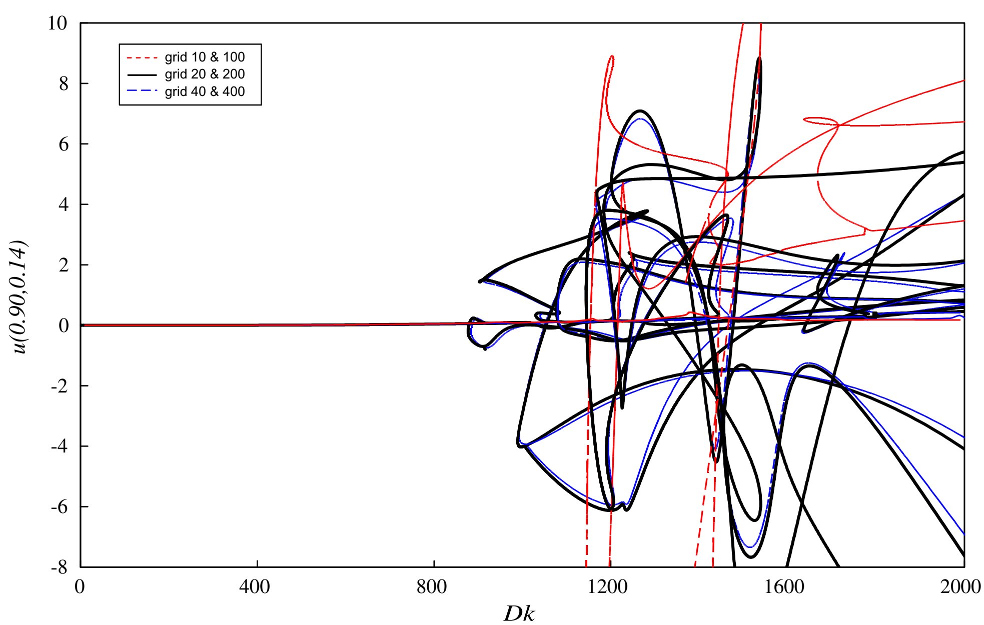

Fig. 2. Effect of grid sizes on bifurcation structures.

Table 1
Location variation of some limit and bifurcation points in terms of their *De* values with grid size.

Points	Grids	*De*	Points	Grids	*De*
S_2^1	10 × 100	\	S_4^5	10 × 100	\
	20 × 200	113.62		20 × 200	124.27
	40 × 400	114.12		40 × 400	124.74
S_3^5	10 × 100	200.11	S_5^5	10 × 100	\
	20 × 200	155.48		20 × 200	148.03
	40 × 400	155.45		40 × 400	147.77
S_4^1	10 × 100	\	S_5^6	10 × 100	\
	20 × 200	132.42		20 × 200	139.24
	40 × 400	133.16		40 × 400	138.94
S_4^3	10 × 100	\	S_7^1	10 × 100	\
	20 × 200	115.91		20 × 200	141.34
	40 × 400	116.76		40 × 400	140.98
S_4^4	10 × 100	148.03	A_1^1	10 × 100	\
	20 × 200	156.61		20 × 200	136.12
	40 × 400	155.24		40 × 400	136.01

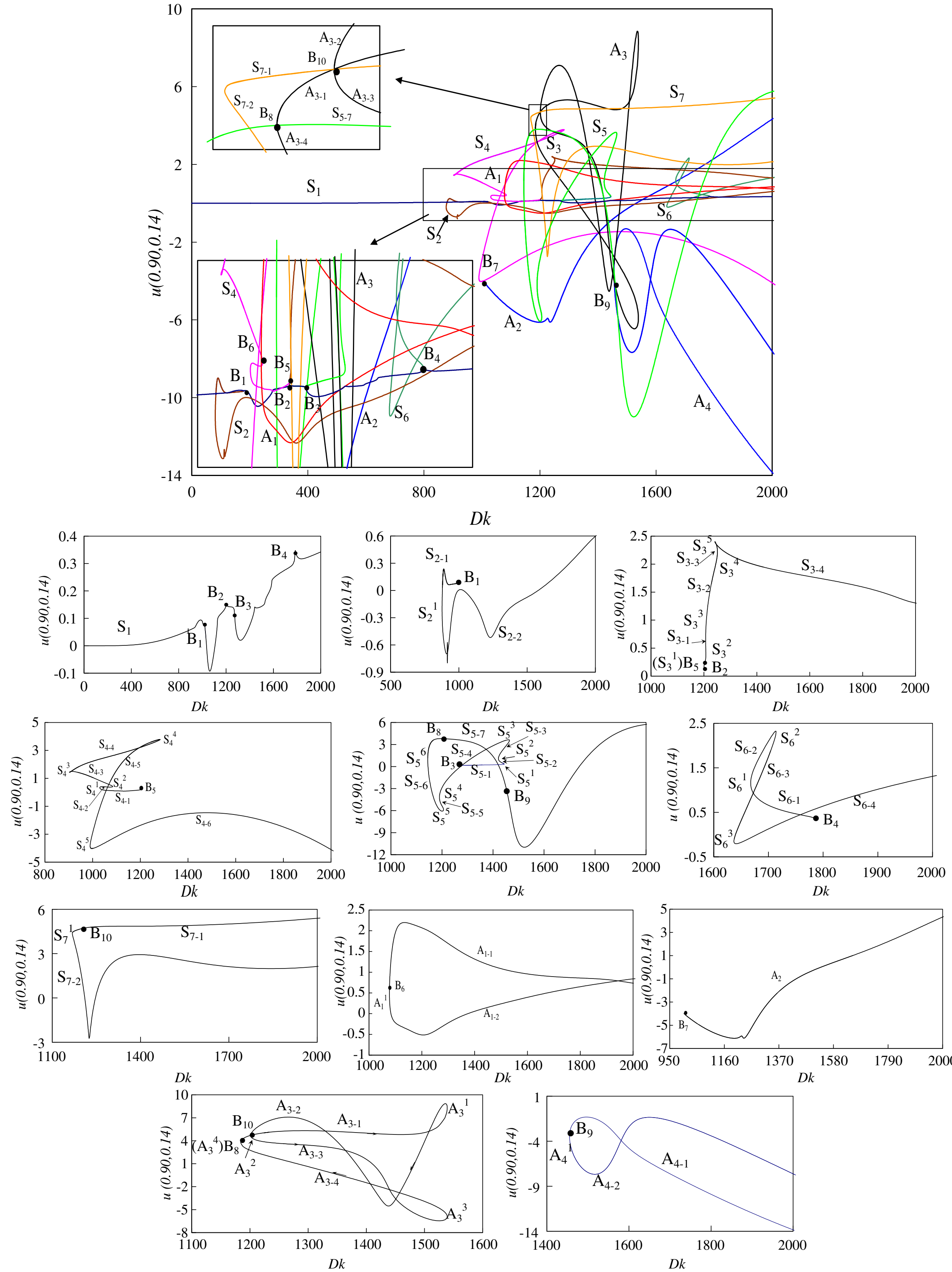

Fig. 3. Solution branches and their connectivity.

Continuity equation:

$$\frac{\partial}{\partial r}\left\{\left[1+\sigma\frac{4r-(1+1/\gamma)}{4}\right]u\right\}+\frac{\partial}{\partial z}\left\{\left[1+\sigma\frac{4r-(1+1/\gamma)}{4}\right]v\right\}=0 \tag{6}$$

Momentum equations:

$$\frac{\partial u}{\partial \tau}+u\frac{\partial u}{\partial r}+v\frac{\partial u}{\partial z}-\frac{16w^2Dk^2}{\sigma\{1+\sigma[r-(1+1/\gamma)/4]\}} =-\frac{\partial p}{\partial r}+\left\{\frac{\partial^2 u}{\partial r^2}+\frac{\partial^2 u}{\partial z^2}+\frac{\sigma}{1+\sigma[r-(1+1/\gamma)/4]}\frac{\partial u}{\partial r}-\frac{\sigma^2 u}{[1+\sigma(r-(1+1/\gamma)/4)]^2}\right\}, \tag{7}$$

$$\frac{\partial v}{\partial \tau}+u\frac{\partial v}{\partial r}+v\frac{\partial v}{\partial z}=-\frac{\partial p}{\partial z}+\left\{\frac{\partial^2 v}{\partial r^2}+\frac{\partial^2 v}{\partial z^2}+\frac{\sigma}{1+\sigma[r-(1+1/\gamma)/4]}\frac{\partial v}{\partial r}\right\}, \tag{8}$$

$$\frac{\partial w}{\partial \tau}+u\frac{\partial w}{\partial r}+v\frac{\partial w}{\partial z}+\frac{\sigma u w}{1+\sigma[r-(1+1/\gamma)/4]} =\frac{1}{1+\sigma[r-(1+1/\gamma)/4]} +\left\{\frac{\partial^2 w}{\partial r^2}+\frac{\partial^2 w}{\partial z^2}+\frac{\sigma}{1+\sigma[r-(1+1/\gamma)/4]}\frac{\partial w}{\partial r}-\frac{\sigma^2 w}{[1+\sigma[r-(1+1/\gamma)/4]]^2}\right\}; \tag{9}$$

Energy equation:

$$\frac{\partial \theta}{\partial \tau}+u\frac{\partial \theta}{\partial r}+v\frac{\partial \theta}{\partial z}-\frac{4wDk}{\sigma \Pr\{1+\sigma[r-(1+1/\gamma)/4]\}} =\frac{1}{\Pr}\left\{\frac{\partial^2 \theta}{\partial r^2}+\frac{\partial^2 \theta}{\partial z^2}+\frac{\sigma}{1+\sigma[r-(1+1/\gamma)/4]}\frac{\partial \theta}{\partial r}\right\}. \tag{10}$$

Here the dimensionless variables are defined by [19,20]

$$r=\frac{R}{d_h},\ z=\frac{Z}{d_h},\ \tau=\frac{t}{\nu/d_h^2},\ u=\frac{d_hU}{\nu},\ v=\frac{d_hV}{\nu},\ w=\frac{W}{W_1},$$
$$p=\frac{P}{\rho(\nu/d_h)^2},\ \theta=\frac{T_w-T}{\Delta T},$$

where $W_1=\frac{d_h^2c_1}{\mu}$, c_1 is a positive constant for hydrodynamically fully-developed flow. In $\Delta T=Prd_hc_2$, $c_2=\frac{\partial T}{R_c\partial\phi}$ (a positive constant when the fluid is heated and a negative constant when the fluid is cooled [21,22]). W_1 and ΔT are used for the non-dimensionalization of the axial velocity and temperature respectively as in Yang [23].

σ, γ, Pr and Dk are the four dimensionless parameters. σ and γ are geometrical parameters. Pr is a thermophysical property paramete. Dk is the dynamic parameter that is the ratio of the square root of the product of inertial and centrifugal forces to the viscous force, and characterizes the effect of inertial and centrifugal forces [19,21,24].

Boundary conditions (non-slip, impermeability and uniform peripheral temperature) may be written as, in terms of dimensionless variables,

$$u=v=w=\theta=0 \text{ at } r=0,\ \frac{1}{2}\left(1+\frac{1}{\gamma}\right),\quad \text{for } -\frac{1}{4}(1+\gamma) \le z\le\frac{1}{4}(1+\gamma), \tag{11}$$

$$u=v=w=\theta=0 \text{ at } z=-\frac{1}{4}(1+\gamma),\ \frac{1}{4}(1+\gamma),\quad \text{for } 0\le r \le\frac{1}{2}\left(1+\frac{1}{\gamma}\right). \tag{12}$$

The governing Eqs. (6)–(10) under the boundary conditions (11) and (12) are solved without unsteady terms for the steady bifurcation structure, and then solved with unsteady terms for the dynamic stability of multiple solutions to finite random disturbances by direct transient computation. After velocity fields obtained, the Dean number De can be calculated.

For the steady bifurcation structure, the governing differential Eqs. (6)–(10) are discretized under the boundary conditions (11) and (12) by the finite volume method to obtain discretization equations. The discretization equations are solved for parameter-dependence of flow and temperature fields by Euler–Newton continuation with the solution branches parameterized by the pseudo-Dean number Dk or the local variable. The bifurcation points are detected by the test function developed by Seydel [25,26]. The branch switching is made by a scheme that approximates the difference between branches proposed by Seydel [25,26]. The readers are referred to [27] for the numerical details.

For transient computation aiming for the response of multiple steady solutions to the finite two-dimensional random disturbances, we obtain the discretization equations by integrating the governing equations with the time dependent terms over every control volume and over the time period from τ to $\tau+\Delta\tau$ (the finite volume method). The fully implicit method is used because of its superior numerical stability. The system of discretization equations is then solved by the Euler–Newton method by viewing time τ as the continuation parameter. The initial condition at $\tau=0$, which also serves as the starting point of the continuation scheme, is formed by the steady solution $\boldsymbol{y_s}(Dk)$ plus a finite random disturbance. Here, the subscript $\boldsymbol{s}$ denotes the steady solution. The random disturbance is generated by $\boldsymbol{d}^{(k)}\chi^{(k)}\boldsymbol{y_s}(Dk)$. Here $\boldsymbol{d}$ is the maximum percentage of disturbing value over the steady value $\boldsymbol{y_s}$. The superscript k represents the ordinal of the disturbance. χ is a vector whose components take random values from -1 to 1 and are generated by the computer. To examine dynamic responses of a steady solution to different finite random disturbances, we normally generate three sets of disturbances denoted by $k=1$, 2, and 3, with $d=10\%$, 15%, and 30% respectively. The characteristics of the temporal oscillation are studied by Hilbert spectral analysis [28,29].

The local product of the friction factor and Reynolds number $(fRe)_L$ and Nusselt number Nu_L can be written as [19],

$$(f\mathrm{Re})_L=\frac{2}{w_m}\left(\frac{\partial w}{\partial n}\right)_{wall}, \tag{13}$$

$$Nu_L=\frac{1}{\theta_b}\left(\frac{\partial \theta}{\partial n}\right)_{wall}, \tag{14}$$

Table 2
Locations of all limit and bifurcation points up to $Dk=2000$ at $\sigma=0.5$, $\gamma=10$ and $Pr=7.0$.

Points	Dk	De	Points	Dk	De
S_2^1	876.95	113.62	S_6^2	1713.88	210.44
$S_3^1(B_5)$	1200.00	152.98	S_6^3	1636.95	200.11
S_3^2	1207.30	153.82	S_7^1	1168.53	141.34
S_3^3	1206.48	153.64	A_1^1	1077.53	136.12
S_4^3	1251.02	157.28	A_3^1	1539.07	180.34
S_3^5	1241.30	155.48	A_3^2	1201.34	144.15
S_4^1	1030.21	132.42	A_3^3	1539.04	180.33
S_4^2	1084.14	137.20	$A_3^4(B_8)$	1184.18	142.64
S_4^3	902.35	115.91	A_4^1	1455.17	171.38
S_4^4	1283.19	156.61	B_1	1001.40	128.98
S_4^5	989.37	124.27	B_2	1201.00	153.10
S_5^1	1443.24	181.73	B_3	1270.84	161.43
S_5^2	1421.20	178.84	B_4	1784.60	221.07
S_5^3	1464.63	182.06	B_6	1077.46	136.11
S_5^4	1190.10	147.51	B_7	1003.38	125.57
S_5^5	1206.04	148.03	B_9	1455.28	171.39
S_5^6	1144.23	139.24	B_{10}	1201.25	144.14
S_6^1	1667.57	207.01			

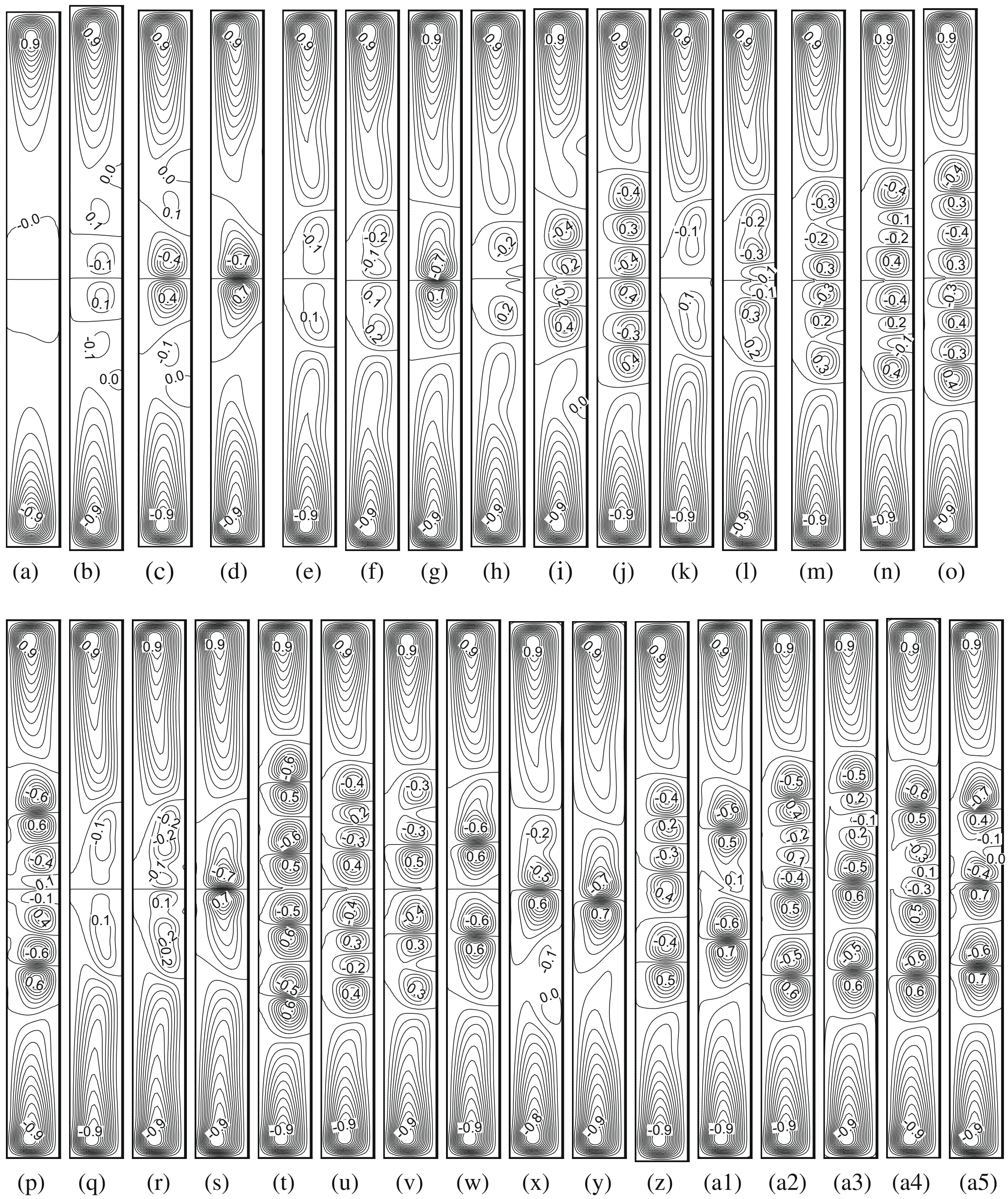

Fig. 4. Typical secondary flows on various solution sub-branches: (a) $Dk = 602$ on S_1; (b) $Dk = 880$ on $S_{2\text{-}2}$; (c) $Dk = 1000$ on $S_{2\text{-}2}$; (d) $Dk = 1500$ on $S_{2\text{-}2}$; (e) $Dk = 1230$ on $S_{3\text{-}2}$; (f) $Dk = 1250$ on $S_{3\text{-}2}$; (g) $Dk = 1500$ on $S_{3\text{-}4}$; (h) $Dk = 1050$ on $S_{4\text{-}2}$; (i) $Dk = 1000$ on $S_{4\text{-}3}$; (j) $Dk = 1000$ on $S_{4\text{-}5}$; (k) $Dk = 1450$ on $S_{5\text{-}3}$; (l) $Dk = 1400$ on $S_{5\text{-}4}$; (m) $Dk = 1200$ on $S_{5\text{-}4}$.; (n) $Dk = 1200$ on $S_{5\text{-}5}$; (o) $Dk = 1150$ on $S_{5\text{-}6}$.; (p) $Dk = 1500$ on $S_{5\text{-}7}$.; (q) $Dk = 1700$ on $S_{6\text{-}2}$; (r) $Dk = 1700$ on $S_{6\text{-}3}$; (s) $Dk = 2000$ on $S_{6\text{-}4}$; (t) $Dk = 1500$ on $S_{7\text{-}1}$; (u) $Dk = 1200$ on $S_{7\text{-}2}$; (v) $Dk = 1250$ on $S_{7\text{-}2}$; (w) $Dk = 1600$ on $S_{7\text{-}2}$; (x) $Dk = 1200$ on $A_{1\text{-}1}$; (y) $Dk = 1500$ on $A_{1\text{-}1}$; (z) $Dk = 1100$ on A_2; (a1) $Dk = 1500$ on A_2; (a2) $Dk = 1400$ on $A_{3\text{-}1}$; (a3) $Dk = 1500$ on $A_{3\text{-}2}$; (a4) $Dk = 1500$ on $A_{4\text{-}2}$; (a5) $Dk = 2000$ on $A_{4\text{-}2}$.

where w_m is the mean dimensionless streamwise velocity, and θ_b is the dimensionless bulk mean temperature. We obtain their average values fRe and Nu by peripherally averaging local values.

3. Grid-dependence check and accuracy check

We check the grid dependence by three pairs of grid sizes, 10×100, 20×200 and 40×400, uniformly distributed in the flow domain. The pair of numbers $(L \times K)$ represents the number of grid points used in r and z directions, respectively. Fig. 2 shows the bifurcation diagrams obtained by these three pair of grid sizes. In Fig. 2, the u velocity component at $r = 0.9$ and $z = 0.14$ is used as the state variable and Dk as the parameter. It shows that the quantitative change is small from 20×200 to 40×400. Table 1 lists location variations of some limit and bifurcation points in terms of their De values as grid sizes. The general trend of these results tends to indicate that the solutions for the case of (20×200) grids are accurate to within 1% tolerance. We also checked the detailed variations of flow and temperature fields on various solution branches for different grid sizes, and found that 20×200 is indeed a reasonably accurate choice for the grid size. It is worth noting that the CPU time increases rapidly as the grid spacing decreases (the computations were carried out on the High Performance Computing (HPC) cluster in the University of Hong Kong).

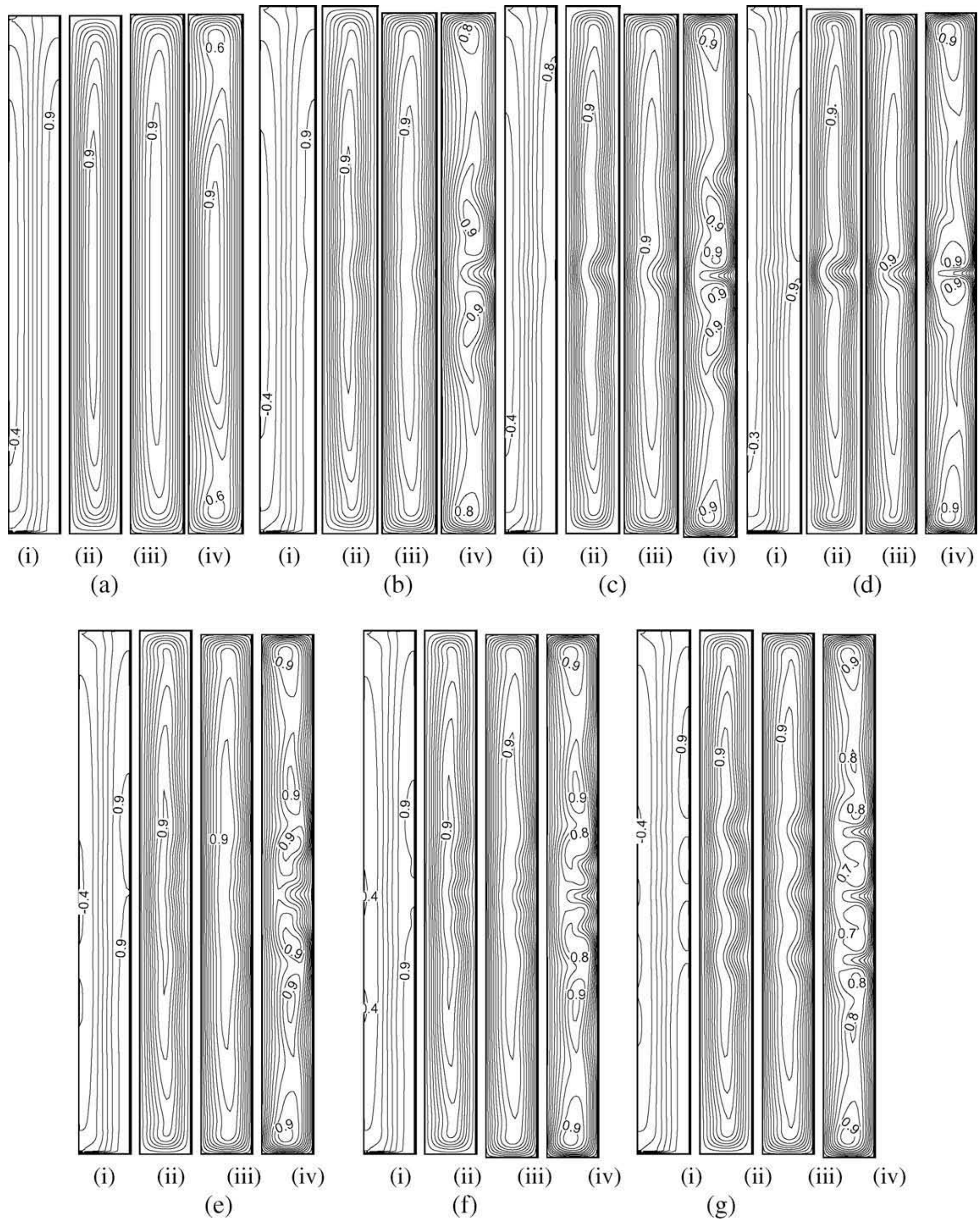

Fig. 5. Flow, temperature, pressure and centrifugal force fields on different branches at different *Dk*: (i) Pressure; (ii) Centrifugal force; (iii) Streamwise velocity; (iv) Temperature; (a) $Dk = 602$ on S_1; (b) $Dk = 880$ on $S_{2\text{-}2}$; (c) $Dk = 1000$ on $S_{2\text{-}2}$; (d) $Dk = 1500$ on $S_{2\text{-}2}$; (e) $Dk = 1230$ on $S_{3\text{-}2}$; (f) $Dk = 1250$ on $S_{3\text{-}2}$; (g) $Dk = 1000$ on $S_{4\text{-}5}$.

Therefore, all our computations are made with a 20×200 uniform mesh in order to have a balance between the computational cost and the solution accuracy. The details of accuracy check are available in [27].

4. Results and discussion

4.1. Flow structures

The Solution branches and their connectivity are shown in Fig. 3 where *S* stands for symmetric solutions with respect to the horizontal central plane $z = 0$ and *A* for asymmetric solutions. Limit points of the branches are denoted by their branch symbol with a superscript number and bifurcation points are denoted by *B* with an ordinal number. For example, S_1^2 represents the second limit point on the solution branch S_1. Eleven solution branches S_1, S_2, S_3, S_4, S_5, S_6, S_7, A_1, A_2, A_3 and A_4 are found in the *Dk* range from 0 to 2000. The primary branch S_1 is symmetric and has four bifurcation points B_1, B_2, B_3 and B_4 that originate four symmetric branches S_2, S_3, S_5 and S_6. Branch S_3 has one bifurcation point B_5, originating a symmetric branch S_4. Branch S_4 has two bifurcation points B_6 and B_7 that generate asymmetric branches A_1 and A_2 respectively. Branch S_5 has two bifurcation points B_8 and B_9, leading to branches A_3 and A_4 respectively. Branch S_7 is connected with branch A_3 at

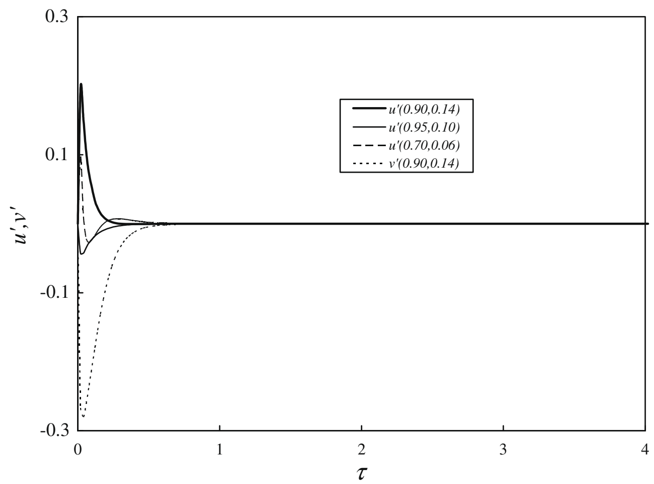

Fig. 6. Dynamic responses of the flow at $Dk = 822$ on S_1 to finite random disturbances: evolution to a stable steady 2-cell flow.

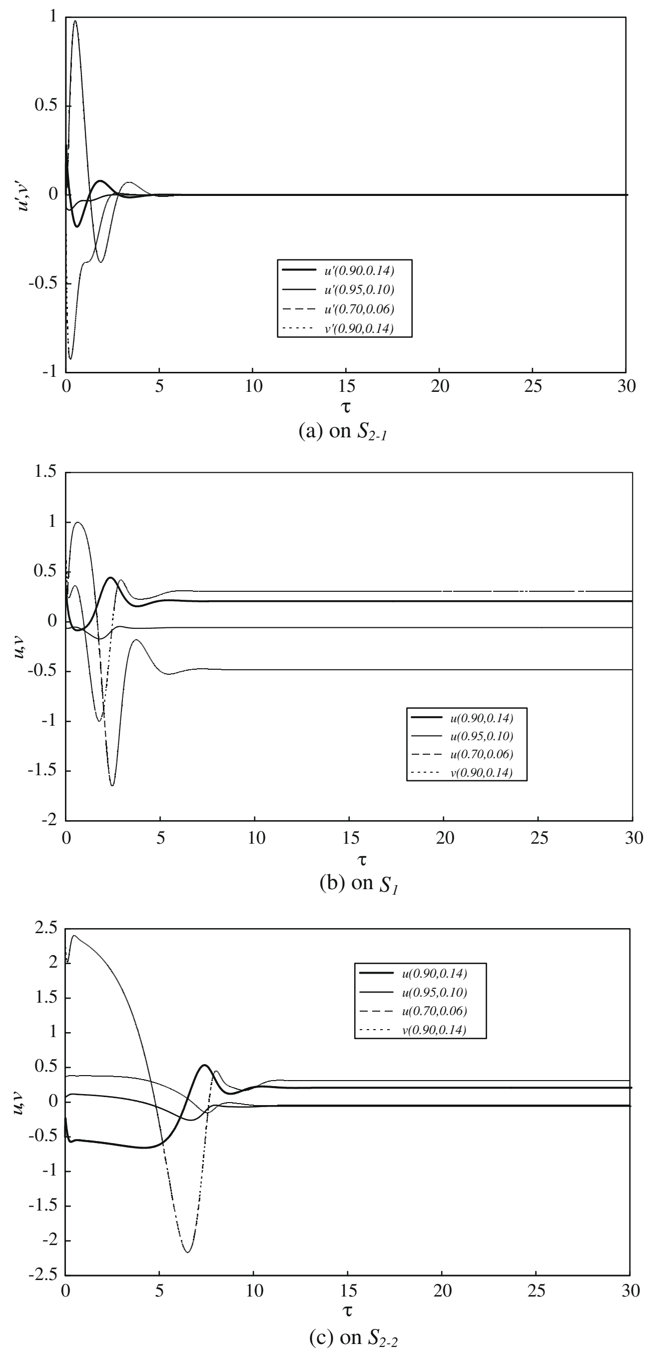

Fig. 7. Dynamic responses of the flows at $Dk = 885$ on $S_{2\text{-}1}$, S_1 and $S_{2\text{-}2}$ to finite random disturbances: evolution to stable steady state on $S_{2\text{-}1}$.

bifurcation point B_{10}. The branch connectivity and some limit points are shown in the locally-enlarged state diagrams in Fig. 3. Each pair of singular points (B_5, S_3^1) and (B_8, A_3^4) represents a single point of higher nullity in the continuous problem. The pair of singular points (B_{10}, A_3^2) are very close. Their slight separation may be an artifact of the numerical discretization. It is noted that all intersecting points except the ten bifurcation points should not be interpreted as connection points in this 1D projection of N dimensional solution branches. Table 2 lists Dk and De values of ten bifurcation points B_1 to B_{10} and 27 limit points.

Symmetric branch S_1. The primary branch S_1 is a symmetric branch with four bifurcation points B_1–B_4 (Fig. 3). The flow structure changes along this branch due to the imbalance between the pressure gradient and the centrifugal force. The typical secondary flows on various solution sub-branches are shown in Fig. 4. A vortex with a positive (negative) value of the secondary flow stream function indicates a counterclockwise (clockwise) circulation. Secondary flow on S_1 is essentially a symmetric 2-cell structure (two Ekman vortices, Fig. 4(a)). The length of two Ekman vortices is three or four times longer than their width. This results from a large duct aspect ratio. Fig. 5 shows the variation of flow, temperature, pressure and centrifugal force fields on various sub-branches with Dk value. The stream function, axial velocity, temperature, pressure and centrifugal force are normalized by their corresponding maximum absolute values $|\psi|_{\max}$, w_{max}, θ_{max}, p_{max} and f_{max} in Figs. 4 and 5. For the flow in Fig. 4(a), the pressure gradient across the duct in the radial direction is positive (Fig. 5(a)–(i)). The centrifugal force acts toward the outer wall and decreases from a maximum value to zero at the wall (Fig. 5(a)–(ii)). The secondary flow driven by centrifugal force affects the streamwise velocity and temperature. Maximum velocity peak appears in the duct core region (Fig. 5(a)–(iii)), which is different from the flow in square curved ducts [30]. Along the upper and lower walls, inward secondary flow brings the relatively cold (non-dimensional temperature close to zero) fluid from the outer wall to the inner wall; the colder fluid from the inner wall flows towards the outer wall, around the core region, and isolates the warmer fluid in the core region and two regions near the upper and lower walls. Thus two temperature valleys appear between two end peaks and the middle peak (Fig. 5(a)–(iv)). This also differs from that in square ducts [30]. As Dk increases, the Ekman vortices become stronger.

Symmetric branch S_2. The primary branch S_1 has a bifurcation point B_1 at $Dk = 1001.40$ ($De = 128.98$). It originates a symmetric solution branch S_2 which is divided into two parts $S_{2\text{-}1}$ and $S_{2\text{-}2}$ by limit point S_2^1 (Fig. 3). Secondary flow on $S_{2\text{-}1}$ is essentially a symmetric 2-cell structure, similar to that in Fig. 4(a) (two Ekman vortices). As Dk increases, the Ekman vortices become stronger. Flow on $S_{2\text{-}2}$ is a symmetric 8-cell structure at low Dk value (one pair of Ekman vortices and three pairs of weak Dean vortices, Fig. 4(b)). The isolines of the pressure and centrifugal force are wave-shaped (Fig. 5(b)–(i), (ii)). In the core region of the duct, the streamwise velocity is distorted and the central temperature peak is divided into two peaks (Fig. 5(b)–(iii), (iv)) due to Dean vortices at the center. As Dk increases, the pair of center Dean vortices grow while the other two pairs of Dean vortices disappear (Fig. 4(c) and (d)). Isovels and isotherms are tightly spaced near the central

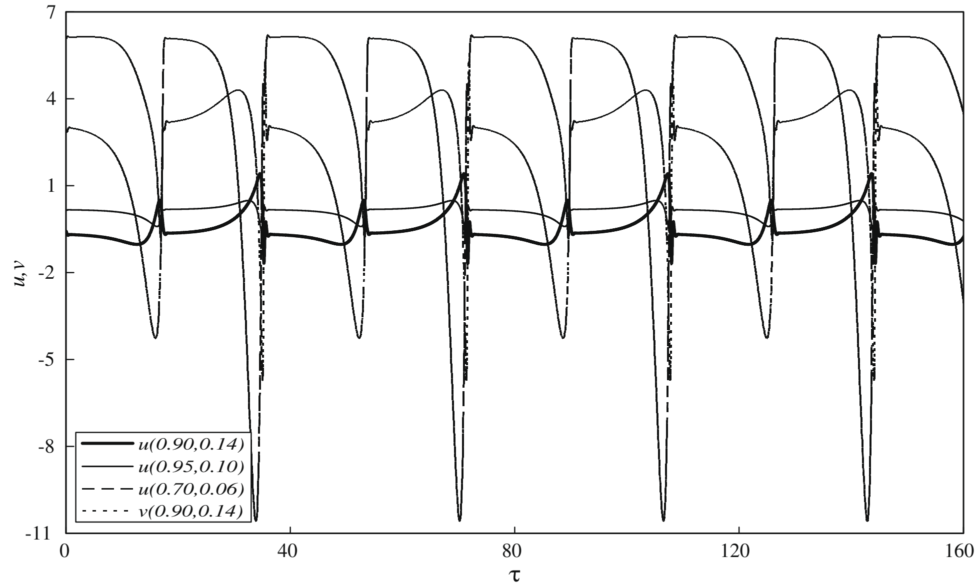

(a) Periodic oscillation (period = 36.34).

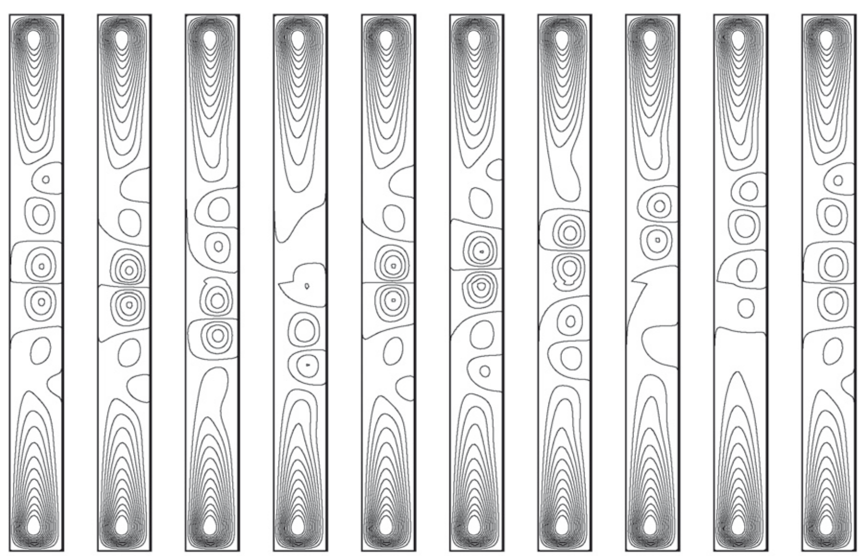

(b) Typical secondary flow patterns during one period of oscillation from solution at $Dk = 900$ on $S_{2\text{-}2}$

Fig. 8. Dynamic responses of flows to finite random disturbances at $Dk = 900$ on $S_{2\text{-}2}$.

inner wall and sparsely spaced near the central outer wall because of the inward secondary flow in the core region of the duct (Fig. 5(b), (c), (d)–(iii) and (b), (c), (d)–(iv)).

Symmetric branch S_3. The primary branch S_1 has a second bifurcation point B_2 at $Dk = 1201.00$ ($De = 153.10$). It yields a symmetric solution branch S^5 which is divided into four sub-branches, $S_{3\text{-}1}$–$S_{3\text{-}4}$, by three limit points $S_3^3, S_3^4 and S_3^5$ (Fig. 3). While the sub-branch $S_{3\text{-}1}$ contributes, through the two limit points S_3^1 and S_3^2, three solutions for any value of Dk in a very small range $1200.00 < Dk < 1207.30$, the difference among these three solutions is negligibly small. Flow on $S_{3\text{-}1}$ is 2-cell, similar to that on $S_{2\text{-}1}$ (Fig. 4(a)). This is due to the similarity of pressure and centrifugal force fields between them. Thus their streamwise velocity and temperature are also similar. Limit point S_3^3 leads to appearance of one pair of Dean vortices in the region near the central outer wall on $S_{3\text{-}2}$ due to the Dean instability (Figs. 4(e) and 5(e)–(i), (ii), [31]). Then another pair of Dean vortices appear because of the splitting of the original pair by the Eckhaus instability (Figs. 4(f) and 5(f)–(i), (ii)). Thus flow on $S_{3\text{-}2}$ is a 6-cell. The flow on $S_{3\text{-}3}$ is also a 6-cell with stronger Dean vortices than those on $S_{3\text{-}2}$. Isovels and isotherms near the inner and outer walls change from smooth to wave-shaped as the Dean vortices appear and grow (Fig. 5(e), (f)–(iii) and (e), (f)–(iv)). Driven by the strong inward secondary flow, the cold fluid flows from the center outer wall to the core region, thus one temperature valley appears in the center of the duct with temperature peaks nearby (Fig. 5(e) and (f)–(iii) and (e) and (f)–(iv)).The limit point S_3^4 leads two pairs of center vortices on $S_{3\text{-}3}$ to merge and become one pair. Thus the flow on $S_{3\text{-}4}$ becomes a 4-cell state (Fig. 4(g)). This is due to the Eckhaus instability.

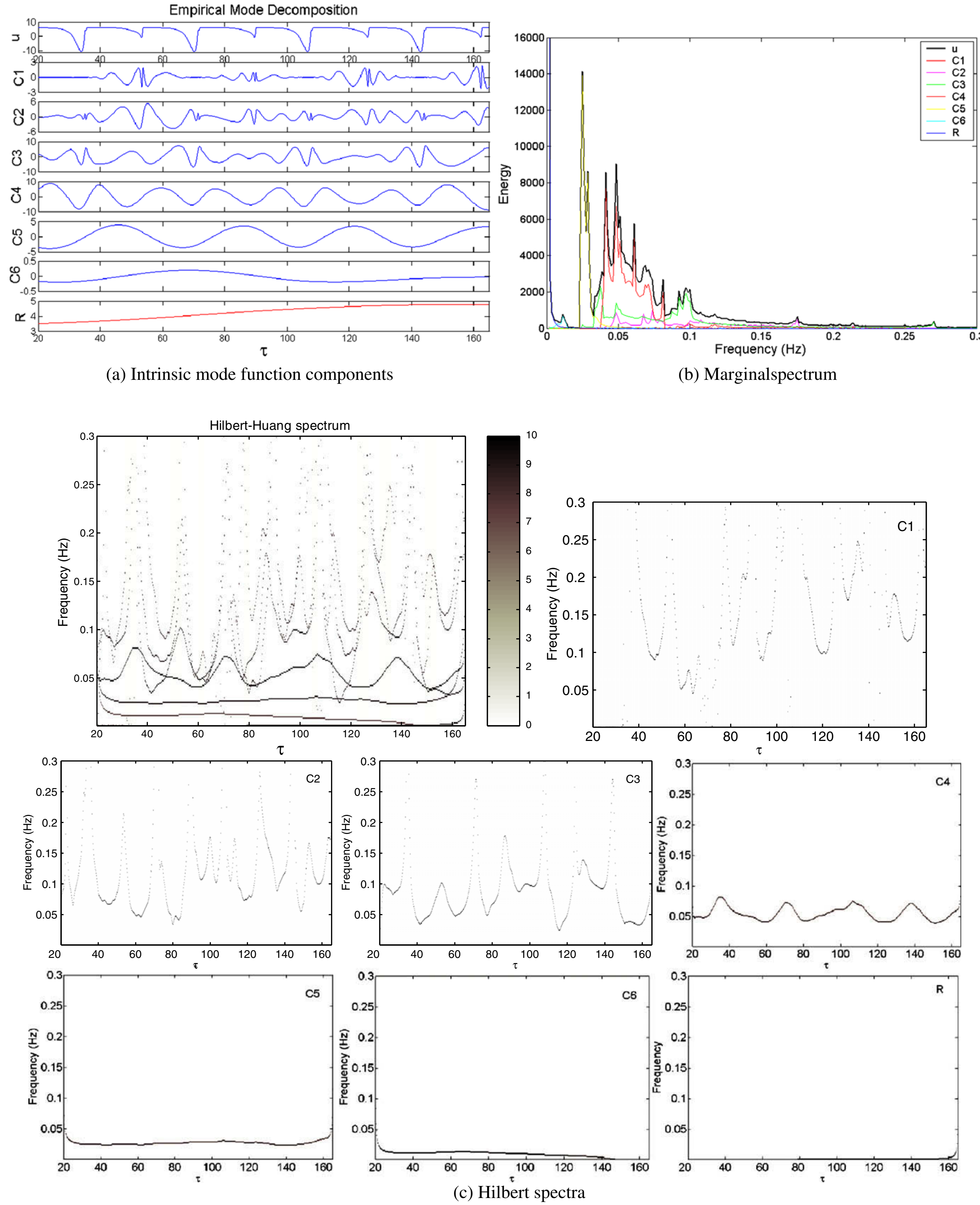

(a) Intrinsic mode function components

(b) Marginalspectrum

(c) Hilbert spectra

Fig. 9. Empirical mode decomposition and Hilbert spectral analysis of the intermittent oscillation *u* (0.90, 0.14) on $S_{2\text{-}2}$ at $Dk = 900$ in Fig. 8 ($20 \leqslant \tau \leqslant 165$).

Symmetric branch S_4. The symmetric branch S_3 has a bifurcation point B_5 at $Dk = 1200.00$ ($De = 152.98$) that yields a symmetric branch S_4^5. Branch S_4 has five limit points $S_4^1 - S_4$ which divide the branch into six parts $S_{4\text{-}1}$–$S_{4\text{-}6}$ (Fig. 3). The flow on $S_{4\text{-}1}$ is 2-cell. The pressure, centrifugal force, streamwise velocity and temperature fields on $S_{4\text{-}1}$ are similar to those on S_1 (Fig. 4(a)). The limit point S_4^1 leads the 2-cell flow on $S_{4\text{-}1}$ to a 4-cell structure on $S_{4\text{-}2}$ (Fig. 4(h)). The flows on $S_{4\text{-}3}$ and $S_{4\text{-}4}$ are 6-cell (Fig. 4(i)). The flows

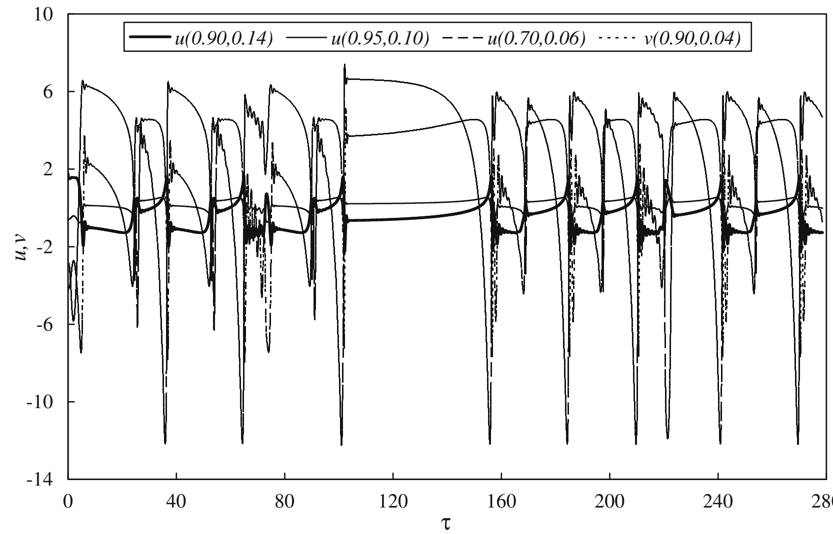

(a) Intermittency oscillation

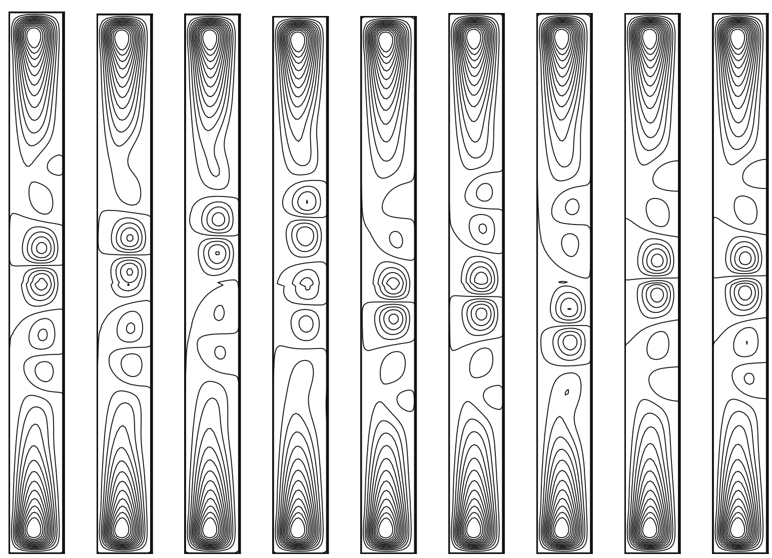

τ = (a)238.59, (b) 240.73, (c) 241.53, (d) 241.88, (e) 242.53, (f) 248.58, (g) 253.67, (h) 255.12, (i) 258.57.

(b) Typical secondary flow patterns during one period of oscillation

Fig. 10. Dynamic responses of flows to finite random disturbances at Dk = 910 on $S_{4\text{-}4}$.

on $S_{4\text{-}5}$ and $S_{4\text{-}6}$ are 8-cell (Fig. 4(j)). Additional Dean vortices occur between two end Ekman vortices on these sub-branches due to the instability. The alternating appearance of counterclockwise- and clockwise-circulating center vortices leads the isovels and isotherms along the inner wall and the outer wall to be wave-shaped through their impinging and retreating effects (Fig. 5(g)–(iii) and (g)–(iv)).

Symmetric branch S_5. The primary branch S_1 has a third bifurcation point B_3 at Dk = 1270.84 (De = 161.43), originating a symmetric solution branch S_5. This branch is divided into seven sub-branches $S_{5\text{-}1}$–$S_{5\text{-}7}$ by six limit points $S_5^1 - S_5^6$ (Fig. 3). The flows on $S_{5\text{-}1}$ and $S_{5\text{-}2}$ are 2-cell. The flow, temperature, pressure and centrifugal force fields on $S_{5\text{-}1}$ and $S_{5\text{-}2}$ are similar to those on S_1 (Fig. 4(a)). One pair of Dean vortices appear in the region near the center of outer wall (Fig. 4(k)). The limit point S_5^3 leads the 4-cell flow on $S_{5\text{-}3}$ (Fig. 4(k)) to be 8-cell on $S_{5\text{-}4}$ (Fig. 4(l)). With the decrease of Dk value, the Dean vortices on $S_{5\text{-}4}$ become stronger and the fourth pair of Dean vortices appear (Fig. 4(m)). The fourth pair is formed from the outer wall. The physical mechanisms responsible for the appearance of the fourth pair and the second pair are different. The flows on $S_{5\text{-}5}$, $S_{5\text{-}6}$ and $S_{5\text{-}7}$ are 10-cell (Fig. 4(n) to (p)). Two center vortices become weak on $S_{5\text{-}7}$ as Dk value increases. Dean vortices appear and change in the shape and size due to the flow instability (Fig. 4(k) to (p)). The isovels and isotherms along the inner wall and outer wall become inwash and outwash in the corresponding region with the clockwise-circulating and counterclockwise-circulating center vortices, similar to those in Fig. 5(g).

Symmetric branch S_6. The primary branch S_1 has a fourth bifurcation point B_4 at Dk = 1784.6 (De = 221.07) that originates a symmetric branch S_6. Branch S_6 is divided into four sub-branches $S_{6\text{-}1}$–$S_{6\text{-}4}$ by three limit points $S_6^1 - S_6^3$ (Fig. 3). The flow on $S_{6\text{-}1}$ is a 2-cell structure, similar to that on $S_{3\text{-}1}$, $S_{4\text{-}1}$ and $S_{5\text{-}1}$. The flow on $S_{6\text{-}2}$ is a 4-cell structure with one pair of Dean vortices in the centeral part of the duct due to the Dean instability (Fig. 4(q)). Limit point S_6^2 leads these Dean vortices to split into three pairs due to the Eckhaus instability [32]. The flow on $S_{6\text{-}3}$ is thus an 8-cell

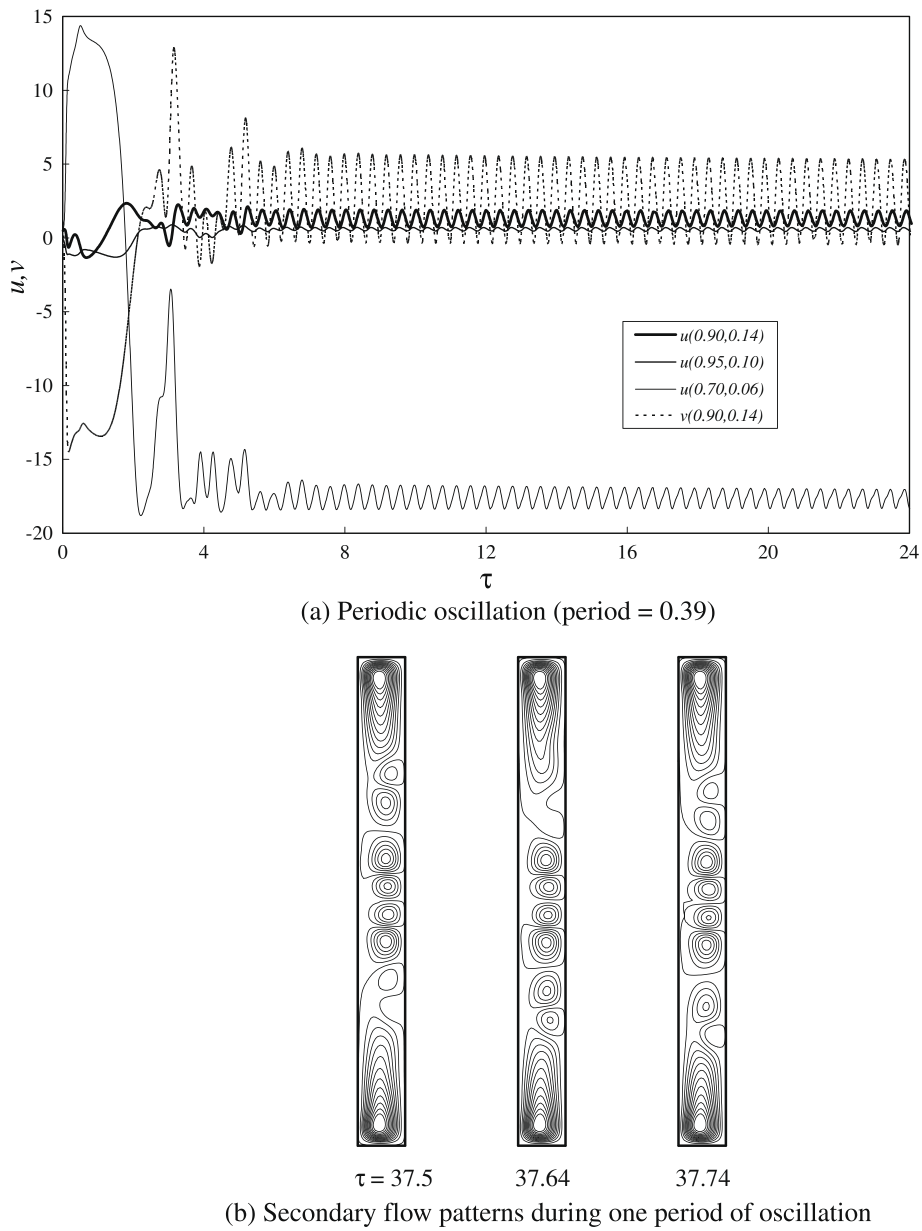

Fig. 11. Dynamic response of flows to finite random disturbances at $Dk = 1000$ on $S_{2\text{-}1}$.

structure (Fig. 4(r)). The limit point S_6^3 leads these three pairs of center cells on $S_{6\text{-}3}$ to merge together due to the Eckhaus instability (Fig. 4(s); [32]). The flow on $S_{6\text{-}4}$ is a 4-cell structure. The isovels and the isotherms change as Dean vortices occur, split apart and merge together along the branch.

Symmetric branch S_7. The branch S_7 is divided into two sub-branches $S_{7\text{-}1}$ and $S_{7\text{-}2}$ by one limit point S_7^1 (Fig. 3). The flow on $S_{7\text{-}1}$ is a 10-cell structure (Fig. 4(t)). Ekman vortices have spanwise extent about two or three times larger than that of the interior Dean cells. The alternate clockwise- and counterclockwise-circulating center vortices lead to wave-shaped isovels and isotherms, similar to those in Fig. 5(g). The flow on $S_{7\text{-}2}$ is 10-cell at low *Dk* value (Fig. 4(u)). With the increase of *Dk* value, the Dean vortices between Ekman vortices and center Dean cells become weak and then merge together due to Eckhaus instability (Fig. 4(v) and (w); [32]). Thus the flow on $S_{7\text{-}2}$ becomes a 6-cell structure at high *Dk* value. The streamwise velocity and temperature vary with the secondary flow structures.

Asymmetric branch A_1. The branch S_4 has one symmetry-breaking bifurcation point B_6 at $Dk = 1077.46$ ($De = 136.11$). This yields an asymmetric solution branch A_1. Branch A_1 has one limit point A_1^1 that divides the branch into upper sub-branch $A_{1\text{-}1}$ and lower sub-branch $A_{1\text{-}2}$ (Fig. 3). The solutions on $A_{1\text{-}2}$ can be formed by mirror images of corresponding solutions on $A_{1\text{-}1}$ at the same *Dk*. Fig. 4(x) and (y) illustrate typical secondary flows at two representative values of *Dk* on $A_{1\text{-}1}$. The flow on $A_{1\text{-}1}$ is a 7-cell structure at low *Dk* value (Fig. 4(x)). With the increase of *Dk* value, the three weak vortices merge into the strong ones nearby and the flow on $A_{1\text{-}1}$ becomes a 4-cell structure due to Eckhaus instability (Fig. 4(y); [32]). Asymmetric secondary flow structures driven by asymmetric pressure and centrifugal forces lead to asymmetric streamwise velocity and temperature profiles.

Asymmetric branch A_2. The branch S_4 has another symmetry-breaking bifurcation point B_7 at $Dk = 1003.38$ ($De = 125.57$). It originates an asymmetric solution branch A_2 (Fig. 3). The flow on A_2 is an 8-cell structure at low *Dk* value (Fig. 4(z)). As *Dk* increases,

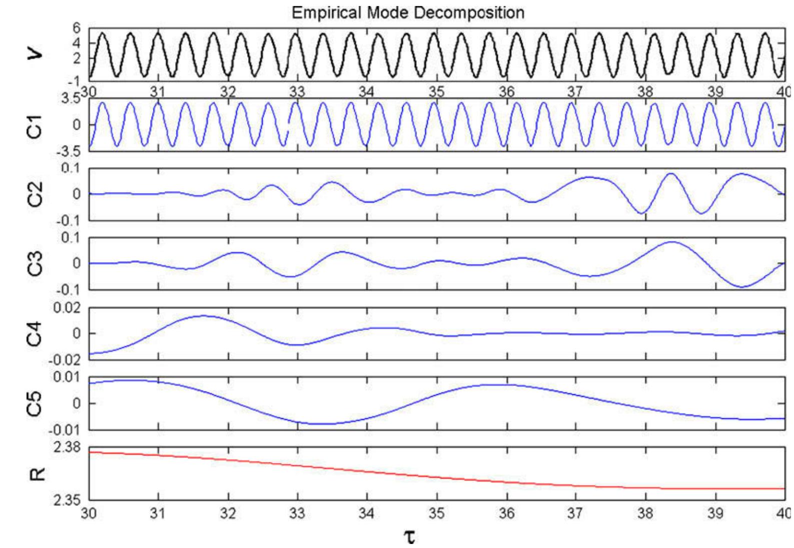

(a) Intrinsic mode function components

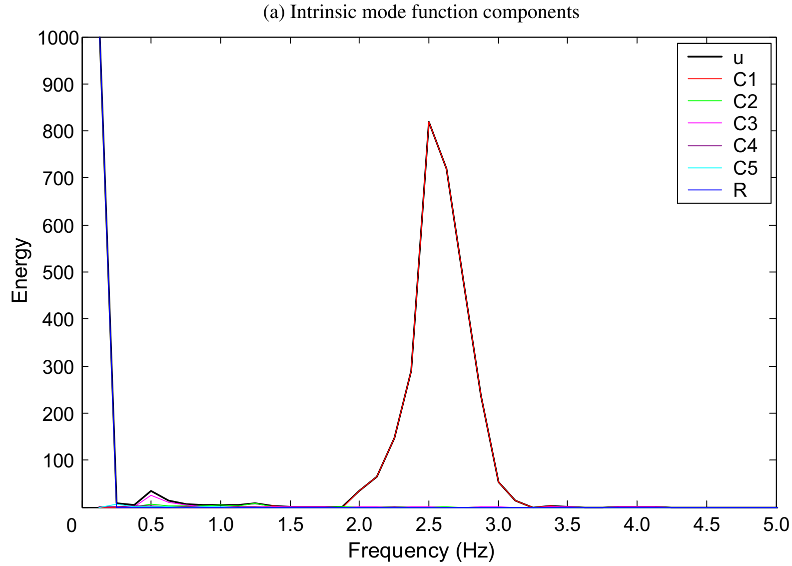

(b) Marginal spectrum

Fig. 12. Empirical mode decomposition and Hilbert spectral analysis of the intermittent oscillation v (0.90, 0.14) on $S_{2\text{-}1}$ at $Dk = 1000$ in Fig. 11(a) ($30 \leqslant \tau \leqslant 40$).

two weak Dean vortices in the upper part of the duct become weak and merge into the strong ones nearby due to Eckhaus instability [32]. Thus the flow on A_2 becomes a 6-cell structure at high Dk value (Fig. 4(a1)). The variation of the secondary flow structure leads the streamwise velocity and temperature fields to change along the branch.

Asymmetric branch A_3. The branch S_5 has a symmetry-breaking bifurcation point B_8 at $Dk = 1184.18$ ($De = 142.64$). It originates an asymmetric closed solution branch A_3 which is connected with S_7 at bifurcation point B_{10} ($Dk = 1201.25$). Branch A_3 is divided into four sub-branches $A_{3\text{-}1}$–$A_{3\text{-}4}$, by four limit points A_3^1–A_3^4 (Fig. 3). The flows on $A_{3\text{-}1}$ and $A_{3\text{-}2}$ are 10-cell asymmetric structures (Fig. 4(a2)–(a3)). As Dk increases, the strength of the Dean vortices on $A_{3\text{-}2}$ changes, some cells become weaker while others become stronger. The flow asymmetry becomes stronger due to the strong instability. The asymmetry of the streamwise velocity and temperature profiles becomes stronger at the same time. The solutions on $A_{3\text{-}3}$ and $A_{3\text{-}4}$ can be formed by mirror images of corresponding solutions on $A_{3\text{-}2}$ and $A_{3\text{-}1}$ at the same Dk respectively.

Asymmetric branch A_4. The branch S_5 has another symmetry-breaking bifurcation point B_9 at $Dk = 1455.28$ ($De = 171.39$), originating an asymmetric solution branch A_4. Branch A_4 has one limit point A_4^1 that divides the branch into upper sub-branch $A_{4\text{-}1}$ and lower sub-branch $A_{4\text{-}2}$ (Fig. 3). The flow on A_4 is a 10-cell asymmetric structure (Fig. 4(a4) and (a5)). The solutions on $A_{4\text{-}2}$ can be formed by mirror images of corresponding solutions on $A_{4\text{-}1}$ at the same Dk. With the increase of Dk value, the strength of the Dean vortices changes. The streamwise velocity and temperature fields change at the same time.

4.2. Flow stability and spectral analysis

The flow response to the disturbances depends on Dk values. As Dk increases, the nonlinearity becomes stronger, thus the finite random disturbances lead the flows from stable to unstable. To examine the dynamic responses of the flows to different finite random disturbances at different Dk values, a relatively comprehensive transient computation is made for 70 typical steady flows with three sets of finite random disturbances with $d = 10\%$, 15% and 30% respectively. We present the results obtained from the disturbance with $d = 30\%$. To illustrate dynamic responses of multiple flows to the finite random disturbances, the deviation of velocity

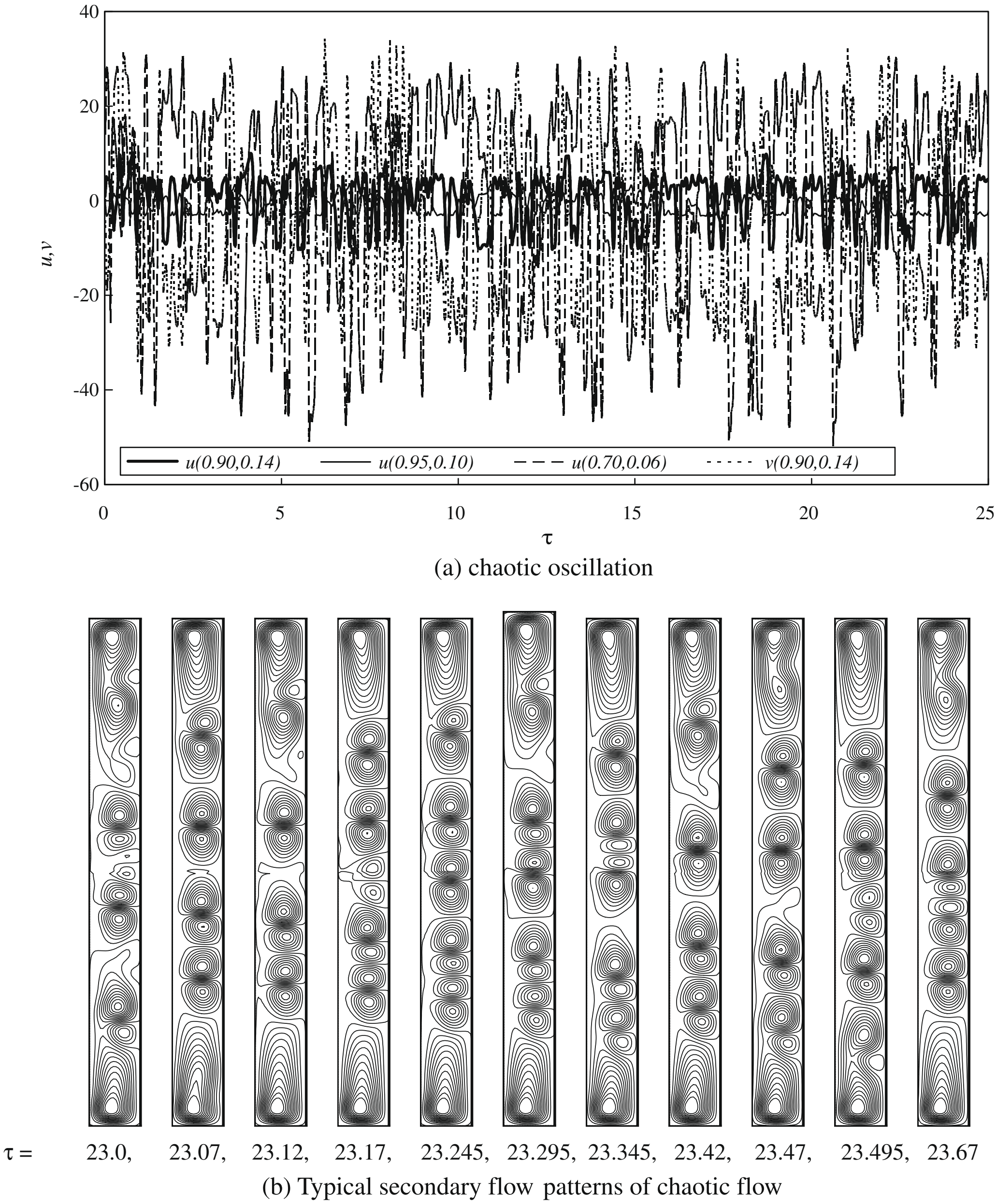

Fig. 13. Dynamic response of flows to finite random disturbances at $Dk = 1500$ on $S_{2\text{-}2}$.

components from their initial steady values is plotted against the time τ at (0.9, 0.14), (0.95, 0.10) and (0.70, 0.06). Radial (*u*-) and spanwise (*v*-) velocity components for the first point (0.9, 0.14) while only *u*- velocity component for the last two points (deviation velocity (u', v') from its initial steady values) are plotted in all figures to facilitate the compassion. The power spectra of temporal oscillations are constructed by the empirical mode decomposition and the Hilbert spectral analysis to confirm the oscillating flow states and reveal their characteristics.

Sub-range 1: stable steady 2-cell state ($0 < Dk \leqslant 876.95$). Only one solution exists at low *Dk* values due to the weak flow nonlinearity. The typical responses of flows on S_1 to the finite random disturbances in this sub-range are shown in Fig. 6. It is observed that at $Dk = 822$ the deviation velocities vanish after a short period time (Fig. 6). The velocity and temperature profiles return to their initial steady 2-cell ones (similar to those in Fig. 4(a)). Therefore, the flow on S_1 is stable with respect to finite random disturbances in the sub-range $0 < Dk \leqslant 876.95$.

Sub-range 2: another stable steady state ($876.95 < Dk < 890$). As *Dk* value increases beyond 876.95 (S_2^1), the stable branch transits from S_1 to $S_{2\text{-}1}$. The dynamic responses of the flows at $Dk = 885$ on S_1, $S_{2\text{-}1}$ and $S_{2\text{-}2}$ to the finite random disturbances are shown in Fig. 7. It is observed that the deviation velocities vanish after a short period time in Fig. 7(a). The velocity and temperature profiles return to their initial steady 2-cell ones (similar to those in Fig. 4(a)). Therefore, the flows on $S_{2\text{-}1}$ are stable with respect to finite random disturbances in the sub-range $876.95 < Dk < 890$. Fig. 7(b) and (c) illustrate the typical responses of the flows on S_1 and $S_{2\text{-}2}$ to the finite random disturbance. It shows that the finite random disturbances lead the flows on S_1 and $S_{2\text{-}2}$ to the stable solution on $S_{2\text{-}1}$ at the same *Dk* in this sub-range. This is also be confirmed by our detailed check of flow and temperature fields. Therefore, the flows on branch S_1 and $S_{2\text{-}2}$ are unstable to the finite random disturbances and respond the disturbances by evolving to the stable solution on $S_{2\text{-}1}$ at the same *Dk* in this sub-range.

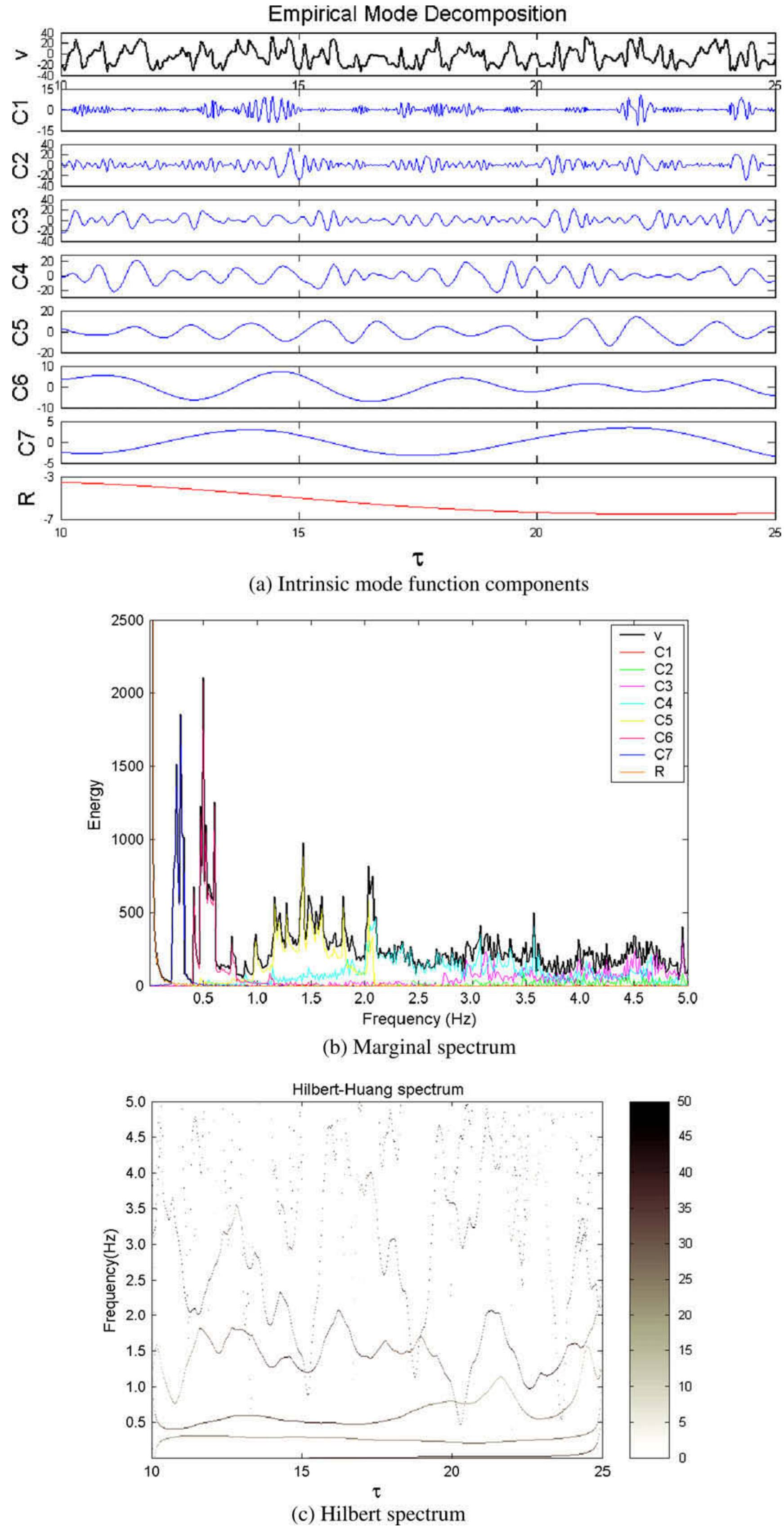

Fig. 14. Empirical mode decomposition and Hilbert spectral analysis of the chaotic oscillation v (0.90, 0.14) on $S_{2\text{-}2}$ at $Dk = 1500$ in Fig. 13(a) ($10 \leqslant \tau \leqslant 25$).

Sub-range 3: periodic oscillations ($890 \leqslant Dk \leqslant 900$). Fig. 8(a) shows that the finite random disturbance lead the flow $S_{2\text{-}2}$ at $Dk = 900$ to oscillations with a period of 36.34. Fig. 8(b) shows some typical secondary flow patterns within one period of oscillation in Fig. 8(a). It is observed that the temporal oscillation is among symmetric/asymmetric 5-cell, 6-cell and 8-cell flows. Further study confirms that the flow and temperature fields within one period of the oscillations are different at different Dk values in the sub-range $890 \leqslant Dk \leqslant 900$. Fig. 9 shows empirical mode decomposition components and Hilbert spectral analysis for periodic oscillation u (0.90, 0.14) on $S_{2\text{-}2}$ at $Dk = 900$ in Fig. 8. It is decomposed into six IMF components and a residue (Fig. 9(a)). IMF components C_1 to C_3 contain fine scales. The dominant time scale is represented by the fifth IMF component C_5, a uniform period of approximately 36.34. This shows that the flow oscillation is periodic. Low-frequency IMF component C_6 represents the low-intensity subharmonics. Residue R is a monotonic component. The Hilbert marginal spectrum in Fig. 9(b) shows C_3 and C_4 carry the most of energy in a large frequency range. The energy peak of frequency 0.0275 Hz represents the temporal scale of the oscillation, indicating the flow oscillation being periodic. There are also some small amplitude noises that are possibly the signature of initial disturbances. Fig. 9(c) shows the Hilbert spectra of the oscillation and its IMF components. In the Hilbert spectra, the IMF components C_1 to C_4 are represented by oscillatory lines indicating that the frequencies vary with time. A detailed comparison among components C_1 to C_4 and their Hilbert spectra shows that the flow has uneven frequency variations even within one period, presenting intra-wave frequency modulations. C_5 is an oscillation with a nearly-constant frequency about 0.0275 Hz. C_6 is a weak sub-harmonic oscillation with low frequency. Therefore the periodic flow oscillation consists of one dominant temporal oscillation, intra-wave frequency modulations and one sub-harmonic oscillation.

Sub-range 4: intermittent oscillations ($900 < Dk \leqslant 980$). As Dk value increases, the stability of the flows changes. Fig. 10(a) shows the dynamic responses of the flows on $S_{4\text{-}4}$ at $Dk = 910$ and on $S_{2\text{-}2}$ at $Dk = 920$ to the finite random disturbances. The finite random disturbances lead the flows to intermittent oscillations. Fig. 10(b) shows some typical secondary flow patterns in Fig. 10(a). It is observed that the flow oscillates among symmetric/asymmetric 6-cell patterns during bursts, but 8-cell patterns during quasi-periodic oscillations.

Sub-range 5: another periodic oscillations ($980 < Dk \leqslant 1350$). The dynamic response of the solution at $Dk = 1000$ on $S_{2\text{-}1}$ is shown in Fig. 11(a). The finite random disturbances here lead the flow to a temporal periodic oscillation with a period of 0.39. Some typical secondary flow patterns are detailed in Fig. 11(b) within one period of oscillation. It is observed that the temporal oscillations are among asymmetric 8-cell, 9-cell and 10-cell flows. Fig. 12 shows empirical mode decomposition components and Hilbert spectral analysis for periodic oscillation v (0.90, 0.14) on $S_{2\text{-}1}$ at $Dk = 1000$ in Fig. 11. It is decomposed into five IMF components and a residue within the window $30 \leqslant \tau \leqslant 40$ (Fig. 12(a)). The first IMF component C_1 contains the dominant time scale with the most energy, a uniform period of approximately 0.39. Low-frequency IMF components C_2 to C_5 represent the low-intensity subharmonics. Residue R is a monotonic component. The Hilbert marginal spectrum in Fig. 12(b) shows one energy peak at the dominant frequency of 2.564 Hz, indicating the flow oscillation being periodic. There are also some small amplitude noises, possibly the signature of initial disturbances.

Sub-range 6: chaotic oscillations ($Dk > 1350$). The finite random disturbances lead the flows in this sub-range to various chaotic oscillations as shown in Fig. 13(a). Fig. 13(b) shows some typical secondary flow patterns in Fig. 13(a). It is observed that the temporal oscillations are among asymmetric 10-cell, 11-cell and 12-cell flows. It is observed that the temporal oscillations on different branches at the same Dk are different. Fig. 14 shows empirical mode decomposition components and Hilbert spectral analysis for chaotic oscillation v (0.90, 0.14) on $S_{2\text{-}2}$ at $Dk = 1500$ in Fig. 13. It is decomposed into seven IMF components and a residue within the window $10 \leqslant \tau \leqslant 25$ (Fig. 14(a)). These IMF components contain different time scales and amplitudes. The residual R is a monotonic component. The Hilbert marginal spectrum in Fig. 14(b) contains the broad-band noise, also indicating the flow being chaotic. The Hilbert spectrum of the chaotic oscillation in Fig. 14(c) shows that the frequencies of the oscillation vary considerably.

Totally six sub-ranges are identified in the Dk range from 0 to 2000 according to the features of dynamic responses to finite random disturbances. The first ranges from $Dk = 0$ to $Dk = 876.95$, where the steady flow on S_1 is stable. In the second sub-range $876.95 < Dk < 890$, finite random disturbances lead all steady flows to the stable steady 2-cell state on $S_{2\text{-}1}$ at the same Dk value. The third covers the range $890 \leqslant Dk \leqslant 900$ where all steady flows evolve to a periodic oscillation. The fourth sub-range is from $Dk = 900$ to $Dk = 980$ where the flows respond to the finite random disturbances in the form of temporal oscillations with intermittency. In the fifth sub-range $980 < Dk \leqslant 1350$, the finite random disturbances lead all solutions to another periodic solution. In the last sub-range $Dk > 1350$, any finite random disturbance will lead the flows to chaotic oscillation. Three sets of finite random disturbances with $d = 10\%$, 15% and 30% lead one steady flow to the same state in the Dk range from 0 to 1350.

4.3. Friction factor and Nusselt number

The average friction factor and Nusselt number on various solution branches are shown in Fig. 15. Even for the same value of Dk and in terms of their average values, both fRe and Nu are different on different solution branches. Sub-branches with many strong Dean vortices such as $S_{4\text{-}6}$ and $S_{7\text{-}1}$ have high values of fRe and Nu. The sub-branches $A_{1\text{-}1}$, $A_{3\text{-}1}$, $A_{3\text{-}2}$ and $A_{4\text{-}1}$ have the same fRe

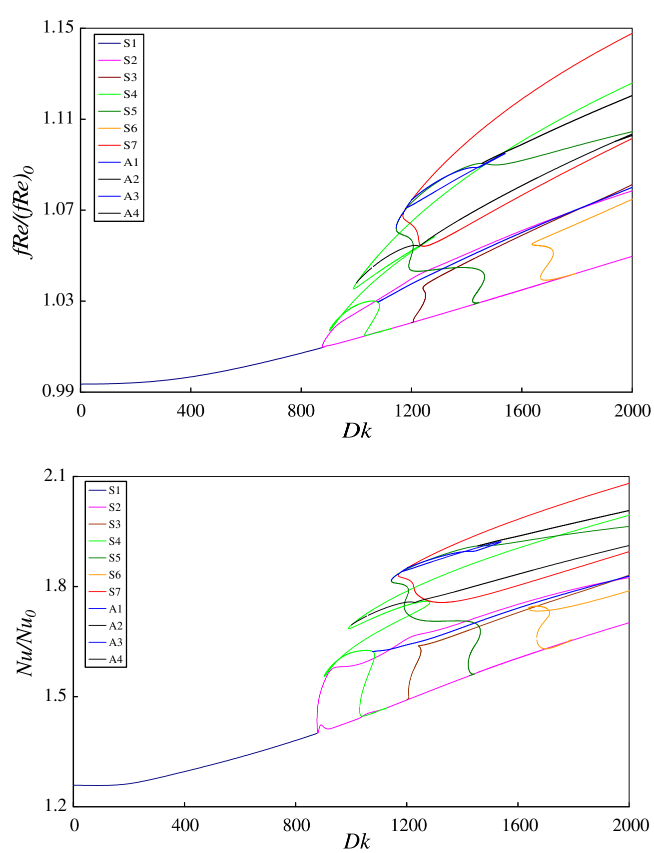

Fig. 15. Average friction factor and Nusselt number on various solution branches.

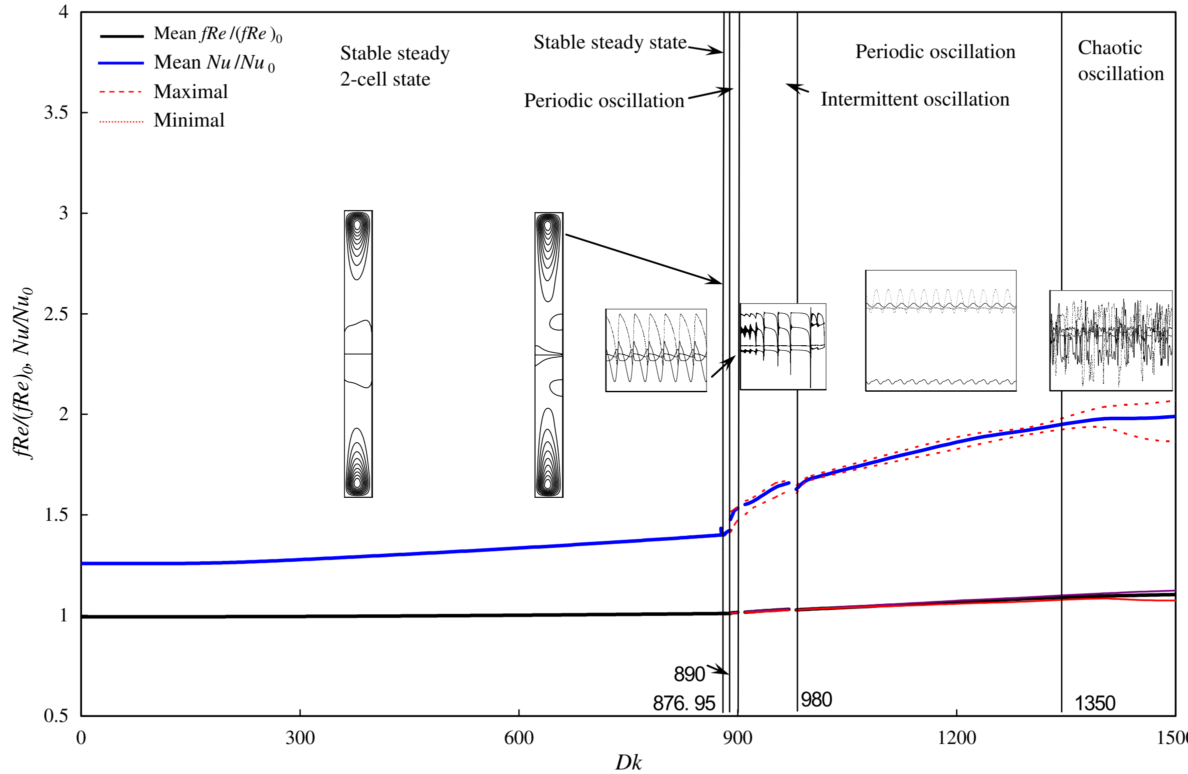

(a) Variations of mean friction factor and mean Nusselt number with Dk

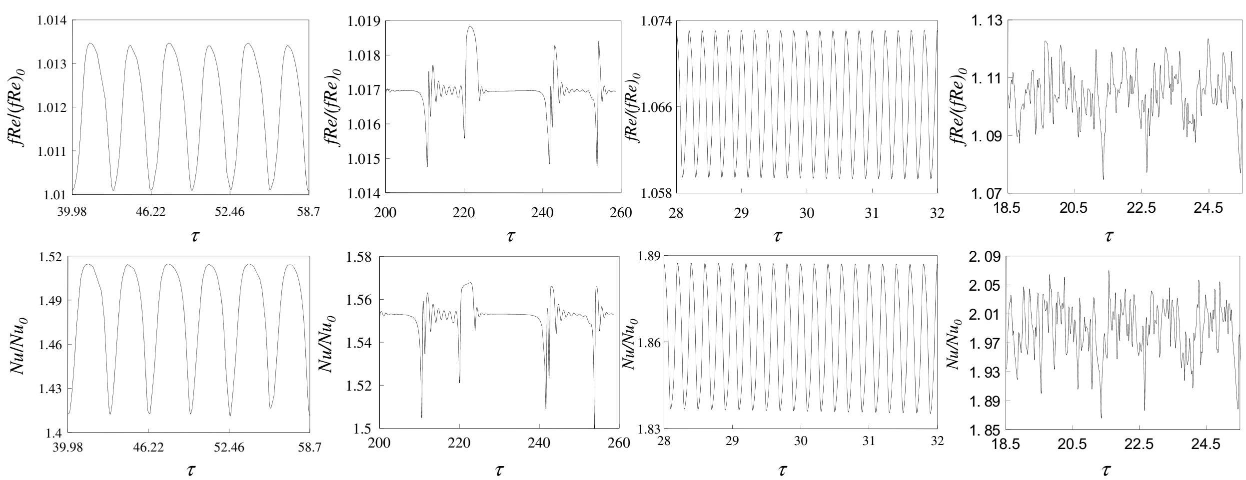

(b) (c) (d) (e)

(b) Periodic oscillation: $Dk = 890$ on $S_{2\text{-}2}$; (c) Intermittent oscillation: $Dk = 910$ on $S_{4\text{-}4}$; (d) Periodic oscillation: $Dk = 1200$ on $S_{5\text{-}4}$; (e) Chaotic oscillation: $Dk = 1500$ on $S_{2\text{-}2}$

Fig. 16. Mean friction factor and mean Nusselt number.

and Nu values as their corresponding sub-branches $A_{1\text{-}2}$, $A_{3\text{-}4}$, $A_{3\text{-}3}$ and $A_{4\text{-}2}$, which are formed by mirror images of $A_{1\text{-}1}$, $A_{3\text{-}1}$, $A_{3\text{-}2}$ and $A_{4\text{-}1}$, respectively. Fig. 15 shows that at $Dk = 2000$ more than 22.33% increase in Nu can be obtained with less than 9.34% increase in fRe due to high curvature ratio and Prandtl number. This is of significant practical importance because the enhancement of heat transfer is much stronger than the increase in the friction.

Fig. 16(a) shows the variations of the spatial mean friction factor and the spatial mean Nusselt number with the Dk number for the physically-realizable flows. For the periodic flows in $890 < Dk \leqslant 900$ and $980 < Dk \leqslant 1350$, the mean friction factor and the mean Nusselt number in Fig. 16(a) are those averaged over one period. They are also averaged over an enough-long period of time for either intermittent flows in $900 < Dk \leqslant 980$ or chaotic flows in $Dk > 1350$. For the oscillating flows in $Dk > 890$, both minimal and maximal values of the mean friction factor and the mean Nusselt number are also shown in Fig. 16(a) with their typical temporal oscillations shown in Fig. 16(b)–(e). The oscillation of the friction factor can in turn induce the oscillation of pumping system. In addition, the thermal stress oscillation caused by the temperature oscillation may result in the failure of equipments [23].

When the flow shifts from stable steady state to temporal oscillation, a drastic change in the mean Nusselt number is observed (Fig. 16(a)). However, the mean friction factor increases quite smoothly as *Dk* increases over the whole range. The transition of mean friction factor and Nusselt number from the second periodic oscillation to the chaotic oscillation is a smooth process. There appears no transition from laminar to turbulent flow for *Dk* up to 1500. Another very interesting feature is that the Nusselt number is much higher than the friction factor for all *Dk* values, and the difference becomes more remarkable as *Dk* increases. We can therefore significantly enhance the heat transfer by the secondary flow in tightly curved rectangular ducts at the expense of very slight increase of resistance to the flow.

5. Concluding Remarks

A numerical study is made on the fully-developed forced convection in tightly coiled rectangular ducts of aspect ratio 10 and curvature ratio 0.5 at Prandtl number 7.0. The governing differential equations from the conservation laws are discretized by the finite volume method and then solved for parameter-dependence of flow and temperature fields by the Euler–Newton continuation. The *Dk* number and the local variable are used as the control parameters in tracing the branches. The test function and branch switching technique are used to detect the bifurcation points and switch the branch respectively. Eleven solution branches (seven symmetric and four asymmetric) are found with 10 bifurcation points and 27 limit points. The flows on these branches are with 2, 4, 6, 7, 8, 9 or 10-cell structures. The flow structures change along the branch because of the flow instability.

The dynamic response of multiple flows and heat transfer to finite random disturbances is examined by the direct transient computation. The finite random disturbances lead the steady flows to a stable symmetric 2-cell flow on S_1 in $0 < Dk < 876.95$, another stable flow on $S_{2\text{-}1}$ in $876.95 < Dk < 890$, a periodic oscillation in $890 \leqslant Dk \leqslant 900$, an intermittent oscillation among symmetric/asymmetric 8-cell flows between two bursts and among symmetric/asymmetric 6-cell flows during the burst in $900 < Dk \leqslant 980$, another periodic oscillation among asymmetric 8-cell, 9-cell and 10-cell flows in $980 < Dk \leqslant 1350$ and a chaotic oscillation in $1350 < Dk \leqslant 2000$. The flow stability changes along the solution branches even without passing any bifurcation or limit points. Hilbert spectral analysis is used to confirm the flow oscillation and reveal its features. Temporal oscillation consists of simple intrinsic modes with different temporal scales and different energy. There is one IMF component with a dominant time scale in a periodic oscillation, the phenomenon not observed for intermittent and chaotic oscillations. The frequencies of the chaotic oscillations vary considerably.

The average friction factor and Nusselt Number are different on different solution branches. It is found that more than 22.33% increase in *Nu* can be achieved with less than 9.34% increase in *fRe* at $Dk = 2000$. Flow oscillations result in temporal oscillations in the friction factor and the Nusselt number. The mean friction factor and mean Nusselt Number are obtained for all physically-realizable flows. A significant enhancement of heat transfer can be obtained at the expense of a slightly increase of flow friction in tightly coiled rectangular ducts.

Acknowledgements

Authors are indebted to Dr. T.L. Yang for his discussion on numerical methods and computer code. The financial support from the Research Grants Council of Hong Kong (GRF7049/06P) to L.W. is gratefully acknowledged.

References

[1] K.C. Cheng, M. Akiyama, Laminar forced convection heat transfer in curved rectangular channels, Int. J. Heat Mass Transfer 13 (3) (1970) 471–490.
[2] G. Yee, R. Chilukuri, J.A.C. Humphrey, Developing flow and heat transfer in strongly curved ducts of rectangular cross-section, J. Heat Transfer – Trans. ASME 102 (2) (1980) 285–291.
[3] Y. Komiyama, F. Mikami, K. Okui, Laminar forced convection heat transfer in curved channel of rectangular cross section, Trans. JSME, Ser. B 50 (1984) 424–434.
[4] P.M. Ligrani, R.D. Niver, Flow visualization of Dean vortices in a curved channel with 40 to 1 aspect ratio, Phys. Fluids 31 (12) (1988) 3605–3617.
[5] S. Thangam, N. Hur, Laminar secondary flows in curved rectangular ducts, J. Fluid Mech. 217 (1990) 421–440.
[6] W.H. Finlay, K. Nandakumar, Onset of 2-dimensional cellular-flow in finite curved channels of large aspect ratio, physics of fluids, Fluid Dyn. 2 (7) (1990) 1163–1174.
[7] P.M. Ligrani, S. Choi, A.R. Schallert, P. Skogerboe, Effects of Dean vortex pairs on surface heat transfer in curved channel flow, Int. J. Heat Mass Transfer 39 (1) (1996) 27–37.
[8] T.T. Chandratilleke, Nursubyakto, Numerical prediction of secondary flow and convective heat transfer in externally heated curved rectangular ducts, Int. J. Thermal Sci. 42 (2) (2003) 187–198.
[9] S. Yanase, K. Nishiyama, On the bifurcation of laminar flows through a curved rectangular tube, J. Phys. Soc. Japan 57 (11) (1988) 3790–3795.
[10] S. Yanase, Y. Kaga, R. Daikai, Laminar flows through a curved rectangular duct over a wide range of the aspect ratio, Fluid Dyn. Res. 31 (3) (2002) 51–183.
[11] S.C.R. Dennis, M. Ng, Dual solutions for steady laminar-flow through a curved tube, Quart. J. Mech. Appl. Math. 35 (Aug) (1982) 305–324.
[12] K. Nandakumar, J.H. Masliyah, Bifurcation in steady laminar-flow through curved tubes, J. Fluid Mech. 119 (Jun) (1982) 475–490.
[13] S. Yanase, N. Goto, K. Yamamoto, Dual solutions of the flow through a curved tube, Fluid Dyn. Res. 5 (3) (1989) 191–201.
[14] K.H. Winters, A bifurcation study of in a curved tube of rectangular cross-section, J. Fluid Mech. 180 (1987) 343–369.
[15] K. Nandakumar, H.J. Weinitschke, A bifurcation study of mixed-convection heat transfer in horizontal ducts, J. Fluid Mech. 231 (1991) 157–187.
[16] S. Yanase, R.N. Mondal, Y. Kaga, Numerical study of non-isothermal flow with convective heat transfer in a curved rectangular duct, Int. J. Thermal Sci. 44 (11) (2005) 1047–1060.
[17] S. Yanase, R.N. Mondal, Y. Kaga, K. Yamamoto, Transition from steady to chaotic states of isothermal and non-isothermal flows through a curved rectangular duct, J. Phys. Soc. Jpn 74 (1) (2005) 345–358.
[18] H. Miyazaki, Combined free and forced convective heat transfer and fluid flow in a rotating curved circular tube, Int. J. Heat Mass Transfer 14 (9) (1971) 1295–1309.
[19] L.Q. Wang, K.C. Cheng, Flow transitions and combined free and forced convective heat transfer in rotating curved channels: the case of positive rotation, Phys. Fluids 8 (6) (1996) 1553–1573.
[20] L.Q. Wang, T.L. Yang, Bifurcation and stability of forced convection in curved ducts of square cross-section, Int. J. Heat Mass Transfer 47 (14–16) (2004) 2971–2987.
[21] H. Miyazaki, Combined free and forced convective heat transfer and fluid flow in a rotating curved rectangular tubes, Int. J. Heat Mass Transfer 95 (1) (1973) 64–71.
[22] S.W. Hong, S.M. Morcos, A.E. Bergles, Analytical and experimental results for combined forced and free convection in horizontal tubes, in: Proceedings of the fifth international heat transfer conference, vol. 3, 1974, pp. 154–158.
[23] T.L. Yang, Multiplicity and stability of flow and heat transfer in rotating curved ducts, Ph.D. thesis, the University of Hong Kong, Hong Kong, China, 2001.
[24] L.Q. Wang, T.L. Yang, Numerical simulation of multiplicity and stability of mixed convection in rotating curved ducts, Int. J. Rotating Mach. 2 (2005) 168–178.
[25] R. Seydel, Branch switching in bifurcation problems for ordinary differential equations, Numerische Mathematik 41 (1) (1983) 93–116.
[26] R. Seydel, Practical Bifurcation and Stability Analysis: From Equilibrium to Chaos, Springer-Verlag, New York, 1994.
[27] L.Q. Wang, F. Liu, Forced convection in slightly curved microchannels, Int. J. Heat Mass Transfer 50 (2007) 881–896.
[28] N.E. Huang, Z. Shen, S.R. Long, M.L.C. Wu, H.H. Shih, Q.N. Zheng, N.C. Yen, C.C. Tung, H.H. Liu, The empirical mode decomposition and the Hilbert spectrum for nonlinear and non-stationary time series analysis, in: Proceedings of the Royal Society of London. Series A, Mathematical Physical and Engineering Sciences, vol. 454, 1998, pp. 903–995.
[29] N.E. Huang, Z. Shen, S.R. Long, A new view of nonlinear water waves: the Hilbert spectrum, Ann. Rev. Fluid Mech. 31 (1999) 417–457.
[30] L.Q. Wang, F. Liu, Forced convection in tightly coiled ducts: bifurcation in a high Dean number region, Int. J. Non-linear Mech. 42 (2007) 1018–1034.
[31] J.T. Stuart, Hydrodynamic Stability, Oxford University Press, 1963.
[32] Y. Guo, W.H. Finlay, Splitting, merging and wavelength selection of vortices in curved and or rotating channel flow due to eckhaus instability, J. Fluid Mech. 228 (1991) 661–691.